Shake-table Tests on Two 40-ton Reinforced Concrete U-shaped Walls with Uniaxial and Bidirectional-Torsional Response

Ryan Hoult[*,a)] M.EERI **António A. Correia,**[b)] **Alex Bertholet,**[a)] **Paulo Candeias,**[b)] **Gwendal Cumunel,**[c)] **Catherine Doneux,**[a)] **Denis Garnier,** [c)] **Yunhyeok Han,**[d)] **Tatjana Isakovic,**[e)] **Antonio Janevski,**[e)] **Stefania Lo Feudo,**[d)] **Andrea Orgnoni,**[f)] **Basile Payen,**[a)] **Dan Palermo,**[g)] **Rui Pinho,**[h)] M.EERI **Filipe Ribeiro,**[b)] **João Pacheco de Almeida**[a)]

Reinforced concrete (RC) structures, widely used in mid- to high-rise construction, face significant challenges related to sustainability, durability, and seismic resilience. Despite extensive experimental research on RC walls, studies specifically focusing on their torsional response remain limited. To address these gaps, the ERIES-ALL4wALL project investigates the torsional and bidirectional flexural behavior of RC U-shaped walls, a key structural feature in contemporary and future high-rise buildings. This paper presents experimental findings from shake-table tests on two slender U-shaped walls, evaluating their nonlinear flexural and torsional performance under realistic seismic ground motions. Advanced instrumentation techniques—such as camera-based vibration measurements—are introduced to capture detailed performance data. The accompanying open-access data is then outlined, enabling further research and development of models to improve the resilience and sustainability of RC core walls in urban environments.

INTRODUCTION

Reinforced concrete (RC) has been the dominant material for medium- to high-rise construction worldwide for over a century, owing to its strength, versatility, and availability. However, its continued use raises urgent environmental and durability concerns. Concrete production is the third-largest source of carbon dioxide emissions globally (Andrew, 2018), and recycling concrete remains costly and inefficient. In Europe alone,

[*]Corresponding author, ryan.hoult@newcastle.edu.au, Laboratoire Essais mécaniques, Bâtiment VINCI, Place du Levant 1, 1348 Louvain-la-Neuve, Belgium.
a) Institute of Mechanics, Materials and Civil Engineering, UCLouvain, Louvain-la-Neuve, Belgium
b) National Laboratory for Civil Engineering (LNEC), Lisbon, Portugal
c) Navier, ENPC, Institut Polytechnique de Paris, Univ Gustave Eiffel, CNRS, Marne-la-Vallée, France
d) QUARTZ Laboratory, Vibrations, Acoustics, Structures and Mechanical Shapes, ISAE-Supméca, Saint-Ouen-sur-Seine, France
e) Faculty of Civil and Geodetic Engineering, University of Ljubljana, Ljubljana, Slovenia
f) University School for Advanced Studies IUSS Pavia, Pavia, Italy
g) Dept. of Civil Engineering, York University, Toronto, ON, Canada
h) Department of Civil Engineering and Architecture, University of Pavia, Pavia, Italy

construction and demolition waste amounts to nearly 500 million tons annually, with concrete comprising roughly one-third of that total (Mália *et al.*, 2013). Moreover, the maintenance, repair, and eventual replacement of RC infrastructure—such as buildings and bridges—will place a heavy financial and environmental burden on future generations (Smil, 2013).

These challenges highlight a broader need: to design concrete structures that are not only more sustainable, but also more durable—capable of serving longer lifespans with lower environmental and economic impacts. Achieving this demands a shift in engineering focus from short-term performance to long-term resilience and serviceability (Flatt *et al.*, 2012). This aligns with a growing societal emphasis on quality and longevity over quantity and disposability (Smil, 2013).

The ERIES-ALL4WALL project—*"Smart ALLoys for WALLs: towards durable structures with long service lives and minimal seismic residual displacements"*—directly responds to these challenges. Funded by the Engineering Research Infrastructures for European Synergies (ERIES) Transnational Access program, the project investigates how innovative materials and wall systems can enhance structural durability while also improving seismic performance. A detailed overview of the project's aims, novel experimental approaches, and collaborative efforts involving seven international research partners and a blind prediction competition can be found elsewhere (Almeida *et al.*, 2024).

Extending the design life of structures, however, presents unique trade-offs. For example, increasing a building's lifespan from 50 to 100 years approximately doubles its probability of experiencing a major earthquake, thereby increasing the required seismic design forces. This paradox—where enhancing long-term utility simultaneously increases disaster exposure—complicates structural design decisions. It also raises critical questions about how to meet the United Nations (2025) Sustainable Development Goal of promoting safety and resilience in disaster risk reduction, especially in the context of rising global seismic risk. While the 20th century saw a general decline in natural disaster fatalities, earthquake-related losses have surged in recent decades, both in lives and economic costs.

In this context, enhancing the seismic resilience of RC buildings is critical. The ERIES-ALL4WALL project focuses on U-shaped RC core walls, a globally common lateral force-resisting system used in mid- and high-rise buildings. These walls will be even more essential in the future, as the global building stock is expected to double by 2060 (UN Environment, 2017) and urban populations grow substantially by 2050. U-shaped RC walls are also foundational in emerging hybrid building types, including tall timber and steel structures, where they provide the necessary stiffness and strength. For instance, landmark timber buildings such as *Ascent* (USA), *HAUT* and *De Karel Doorman* (Netherlands), and *Roots Tower* (Germany) all rely on RC core walls. This trend is likely to extend to even more unconventional structures using materials like bamboo, tree trunks, or fiber-reinforced polymer reinforcement.

Despite significant advances in RC wall research, two key aspects remain underexplored experimentally:

1. Torsional response, which can amplify inelastic demands and damage during seismic events, especially in irregular structures.
2. Residual displacements, which are vital for evaluating post-earthquake repairability and usability.

These two interconnected challenges form the technical focus of the ERIES-ALL4WALL project and are addressed in the sections that follow.

TORSIONAL RESPONSE

During seismic response, all vertical members in a building inevitably experience torsional deformation due to "natural eccentricity" between the center of mass (CM) and either the center of stiffness (CS) during elastic response or the center of resistance (CV) during inelastic response. This torsion occurs even in fully symmetric structures due to "accidental eccentricities" caused by factors such as: (i) non-uniform distribution of live loads; (ii) asymmetric placement of infill walls; (iii) differences between effective member stiffness and design nominal stiffness; (iv) variations in CS along the height of the building; (v) shift in CS during inelastic response; (vi) structural imperfections (Isaković *et al.*, 2021).

Torsion, or twisting, in buildings is a critical mechanism that imposes significant displacement demands on the "flexible side" of the structure. When members yield, torsional stiffness decreases, exacerbating torsion and potentially leading to member failure. Evidence of collapsed or severely damaged structures after strong earthquakes often highlights the critical role of torsional effects.

In RC U-shaped walls, which are much stiffer than other vertical elements, torsion is particularly relevant. Concerns arise due to: (i) significant natural eccentricities in each story, such as having a single peripheral U-shaped wall in regions with low-to-moderate seismic activity (Hoult *et al.*, 2015); (ii) potential amplification of building twist due to differential damage and stiffness degradation in the flanges or web during inelastic response; (iii) significant changes in the center of stiffness (CS) along the height of irregular buildings, sometimes beyond the story's plan perimeter.

While some torsion-related experimental research has focused on RC U-shaped beams for rail viaducts, these findings cannot directly apply to U-shaped walls due to differences in boundary conditions, reinforcement detailing, axial load, and test scale. Only three experimental studies have specifically investigated the torsional capacity of RC walls. Two of these focused on rectangular walls (Peng & Wong, 2011; Türkay & Altun, 2022), with one using monotonic loading. The third study examined H-shaped core walls but used a contentious 1:12 scale factor (Maruta *et al.*, 2000). While there has recently been some experimental testing on RC U-shaped walls (Beyer *et al.*, 2008; Hoult *et al.*, 2020), only small twists were applied to these specimens to provide information on the torsional stiffness, and not on torsional strength.

A recent experimental program led by some of the authors (Hoult *et al.*, 2023b) used reverse-cyclic quasi-static tests to determine the torsional capacity of U-shaped walls. However, a better understanding of the torsional performance of RC U-shaped walls requires evidence from nonlinear dynamic responses, such as shake-table testing. Such need is further emphasized by findings from past experimental research on U-shaped walls, which showed that: (i) the most critical loading direction is the diagonal one (Beyer *et al.*, 2008), and (ii) shear deformation can be significantly larger for U-shaped walls than for rectangular ones (Constantin & Beyer, 2016).

RESIDUAL DISPLACEMENTS

Economic losses from earthquakes often result from excessive residual displacements in structures, which become evident after the ground motion ends. These displacements can cause costly repairs or even demolition and reconstruction. Following major earthquakes, buildings (Marquis *et al.*, 2017) and bridges (Kawashima & Tirasit, 2008) can remain tilted, sometimes imperceptibly. For example, following the 2010–2011 New

Zealand earthquakes, approximately 25 % of buildings in Christchurch's Central Business District (CBD) were deemed uneconomical to repair (Marquis *et al.*, 2017) due to tilts exceeding 25 mm (Muir-Wood, 2015). However, the heights at which some of these tilt measurements were taken were not specified.

Interestingly, many demolitions are not due to structural failure but rather to functional impairments and psychological effects like headaches and dizziness caused by perceived tilts. It is concerning that many demolished structures had performed satisfactorily according to existing regulations, which typically limit lateral displacements or force demands. Even with modern building codes or design standards for concrete structures like those in Europe (CEN, 2004b, 2005), the United States (ACI, 2019), and New Zealand (Standards Association NZ, 2006), countries can still suffer significant economic losses during earthquakes despite low human casualties.

For instance, the Christchurch CBD incurred losses exceeding $NZD 40 billion (20 % of the country's Gross Domestic Product), with about 60 % of multi-story RC buildings demolished and the core business district closed for over two years (Marquis *et al.*, 2017). This has spurred increased analytical and experimental research on residual displacements, with future international design codes likely to include strict limits and revised performance objectives, such as maximum permissible residual drift ratios of 0.5 % (i.e., approximately an angle of 0.3 degrees) (Hoult & Almeida, 2022; McCormick *et al.*, 2008). Instead of a 'life-safe' performance objective, engineers must design buildings to remain serviceable and operational with minimal damage during strong earthquakes. Achieving this requires not only designing for larger seismic loads, as noted in the *Introduction*, but also adopting advanced structural technologies and materials. This study focuses on the latter by exploring a cost-effective reinforcement material—iron-based shape memory alloys—which have the potential to reduce residual displacements. These alloys are used in the second test specimen, as described in the *Description of Test Units* section.

The above restriction may be introduced indirectly via limits to the peak displacement demands, since a relationship between peak inelastic displacements and residual displacements has been recognized for over 40 years (Mahin & Bertero, 1981), and confirmed in numerous subsequent studies (Liossatou & Fardis, 2015). Recent research (Hoult & Almeida, 2022) using a comprehensive dataset of conventional RC wall tests demonstrated a direct correlation: a maximum residual drift ratio of 0.5 % was observed after walls experienced an in-plane drift of approximately 1.5 %.

Thus, poor torsional response of core walls, and consequently the building's increased displacement demands on its flexible side, will likely result in significant non-repairable residual displacements, necessitating demolition.

Although the current work does not, due to brevity, provide a detailed investigation of the residual displacements observed in the experimental results, it is worth noting that some of the authors have examined this topic extensively in other studies (Orgnoni, 2025), namely the relation between residual displacements from quasi-static and dynamic tests.

ERIES-ALL4WALL PROJECT

The ERIES-ALL4wALL project involves shake-table testing of two slender U-shaped walls, designated as UWS1 and UWS2. These walls are subjected to increasing-intensity input motions that induce, in an alternating manner, unidirectional flexure without torsion along the wall weak axis, and bidirectional flexure with torsion. To the authors' knowledge, there have been no previous shake-table tests specifically investigating the torsional response of U-shaped core walls. Some tests have been conducted on U-shaped walls, namely those reported in the previous sections, as well as three U-shaped walls tested at the ELSA laboratory in 2000 (Ile & Reynouard, 2005). However, these were quasi-cyclic tests that did not directly address torsion.

As far as the authors are aware, the only previous shake-table tests on U-shaped walls were performed at the Azalée shake-table at CEA (Ile *et al.*, 2002) using low ductility steel. The primary difference among the three units tested was the spacing of the stirrups, and none considered bidirectional loading or natural eccentricity for torsion. Therefore, the tests herein described are the first to assess the torsional nonlinear dynamic response of U-shaped walls.

The project will concurrently focus on determining (UWS1) and minimizing (UWS2) residual displacements. In this respect, it is noted that the previous Azalée tests showed significant residual displacements. This paper presents key experimental observations and findings from the tests and outlines the organization of the test data, which has been uploaded to a public open-source repository, as detailed in the *Organization of Test Data* and *Summary* sections.

In addition to studying the interaction of torsion and bi-directional flexure in the dynamic response of RC U-shaped core walls, and to investigate, under realistic excitation conditions, a new technology that has the potential to minimize post-earthquake residual displacements, the ERIES-ALL4wALL project had the two following objectives: (i) develop and calibrate numerical models for the walls' response, which was also needed to estimate the behavior of the units prior to the tests; the description of the employed state-of-the-art and state-of-the-practice models will be made in other publications (e.g., Hoult & Almeida, 2024b; Hoult *et al.*, 2025b); (ii) apply innovative instrumentation techniques, including distributed fiber optic sensing (DFOS), camera-based vibration measurements, and a motion capture system; these will also be described in the present paper.

The paper begins by highlighting the significance of the dataset. It then describes the test units, including their geometry, reinforcement layout, material properties, and the experimental setup. An overview of the instrumentation and data acquisition methods are presented, followed by a brief explanation of the similitude laws and the selection of ground motions used. Observations from the tests, including failure modes of both units, are then summarized. The organization of the dataset is subsequently detailed, with example plots provided to illustrate its potential use. The paper concludes with a brief summary and acknowledgements.

DATA SIGNIFICANCE

RC core walls are integral to countless mid- and high-rise buildings worldwide. Despite their popularity, there is limited experimental evidence on the seismic performance of RC U-shaped core walls. Constrained by laboratory limitations, previous investigations by the research community have frequently utilized quasi-static methods, often neglecting explicit considerations of torsional actions. This has hindered the validation of micro- and macro-models of RC buildings with non-planar walls exhibiting torsional response.

The ERIES-ALL4wALL experimental program presented in this paper aims to address these gaps by examining the global and local response of dynamically tested wall units using a shake table. The data obtained is expected to facilitate the validation of numerical models and enhance confidence in computer-aided outputs among engineers and researchers. Additionally, and despite the importance of their economic impact, residual displacements are still almost completely disregarded in Eurocode 8 (CEN, 2004) and many other codes; ERIES-ALL4wALL is expected to promote an explicit consideration of residual displacements, and the need for their minimization, in future code versions.

DESCRIPTION OF TEST UNITS

GEOMETRY AND REINFORCEMENT LAYOUT

The two half-scale U-shaped wall units, denoted UWS1 and UWS2, are identical in geometry. The walls have a thickness (t_w) of 100 mm, with web and flange lengths (L_w and L_f) of 1300 mm and 1050 mm, respectively, as defined in Figure 1. These wall units share the same cross-sectional dimensions as previously tested quasi-static wall units (e.g., Beyer *et al.*, 2008; Constantin & Beyer, 2016; Hoult *et al.*, 2020; Hoult *et al.*, 2023b) but vary with respect to their reinforcement detailing. Differing from previous quasi-static units, these units for dynamic tests have two 100 mm thick intermediate slabs spaced 1.5 m apart, as illustrated in Figure 2. They intend to partially represent the effect of story slabs in the wall response, namely regarding warping and distortion. To the best of the author's knowledge, there is a lack of investigative studies specifically examining the restraint of warping in non-planar walls provided by slabs and other structural elements (e.g., coupling beams). Each slab measures 1900 mm x 1620 mm and is hollow inside the core wall. The slabs were reinforced with two layers of mesh of 6 mm diameter, with a square spacing of 100 mm. The foundation block, measuring 2.1 m x 2.1 m as depicted in Figure 2, was fastened to the shake table floor using sixteen M30 threaded bars evenly spaced at 500 mm orthogonal intervals. A top collar (obtained by considerably increasing the wall thickness at the head) was employed to support the top masses, which is expected to only partially restrain warping (Beyer *et al.*, 2008; Hoult & Almeida, 2024a). The dimensions of the top collar, as shown in Figure 2, include a depth of 500 mm. The wall height, measured from the foundation top to the wall collar and approximately the center of the imposed mass blocks, is 4.54 m (Figure 2) and 5.1 m (Hoult & Almeida, 2024b). Notably, these heights differ from previous quasi-static tests by some of the authors, which had a shear span of 6.72 m (Hoult *et al.*, 2023b).

The design of the test units followed a similar approach to others (e.g., Beyer *et al.*, 2008). Rather than strictly adhering to a specific code, the design prioritized high ductility using capacity design principles deemed reasonable. However, certain aspects, such as longitudinal reinforcement placement, aligned with international building standards for high ductility—e.g., Ductility Class Medium (DCM) or High (DCH) (Varsamis & Papanikolaou, 2021) according to Eurocodes 2 and 8 (CEN, 2004a, 2004b). As shown in Figure 1, the wall units were designed with boundary elements containing a higher concentration of longitudinal and transverse reinforcement to ensure the development of high compressive strains in these regions, necessary for a ductile wall response (Sritharan *et al.*, 2014). The two test units differed in the material used to vertically reinforce these boundary elements: UWS1 was reinforced with 12 mm (Φ12) conventional steel according to Eurocode 8 (CEN, 2004b), as depicted on the right-hand side of Figure 1. In contrast, UWS2 was reinforced with Φ10.7 iron-based shape memory alloys (FeSMA), as depicted on the left-hand side of Figure 1 and explained further in the next section. The FeSMA material was selected to reduce the residual displacements of the wall, as explained in the following section. Additionally, the units differed in the amount of vertical rebars in the boundary elements, commonly expressed in terms of reinforcement ratio (ρ_{wv}), which is the ratio of the area of the lumped longitudinal rebars to the area of concrete in the boundary regions. For example, the flange boundary ends of UWS1, detailed with 6 × 12 mm steel rebars, have a ρ_{wv} of approximately 2.3 %, whereas the 7 × 10.7 mm FeSMA rebars (with an effective area of 89.9 mm^2) in UWS2 result in a ρ_{wv} of 2.1 %. The 4 × 12 mm steel rebars at each web-flange intersection of UWS1 was replaced by 5 × 10.7 mm FeSMA rebars in UWS2. The specific amount of longitudinal reinforcement in each wall was chosen to achieve similar strengths, as predicted from sectional analyses.

The FeSMA rebars extend from the foundation to a lap-splicing region above the first slab. Within the ground-story height (i.e., below the first-story slab), they were shrink-wrapped to promote unbonded behavior with the concrete. The length of this debonded region for specimen UWS2 is shown in Figure 2. Only the rebar ends, i.e. along the foundation and the lap-splice region, remained effectively anchored (i.e., bonded), preventing the strain recovery resulting from the heating process that will be described after; instead, the shape memory effect induced by heating results in recovery stress and the prestressing of the wall. A detailed description of the FeSMA material, including the heating process and its role in inducing the shape memory effect, is provided in the next section.

a)

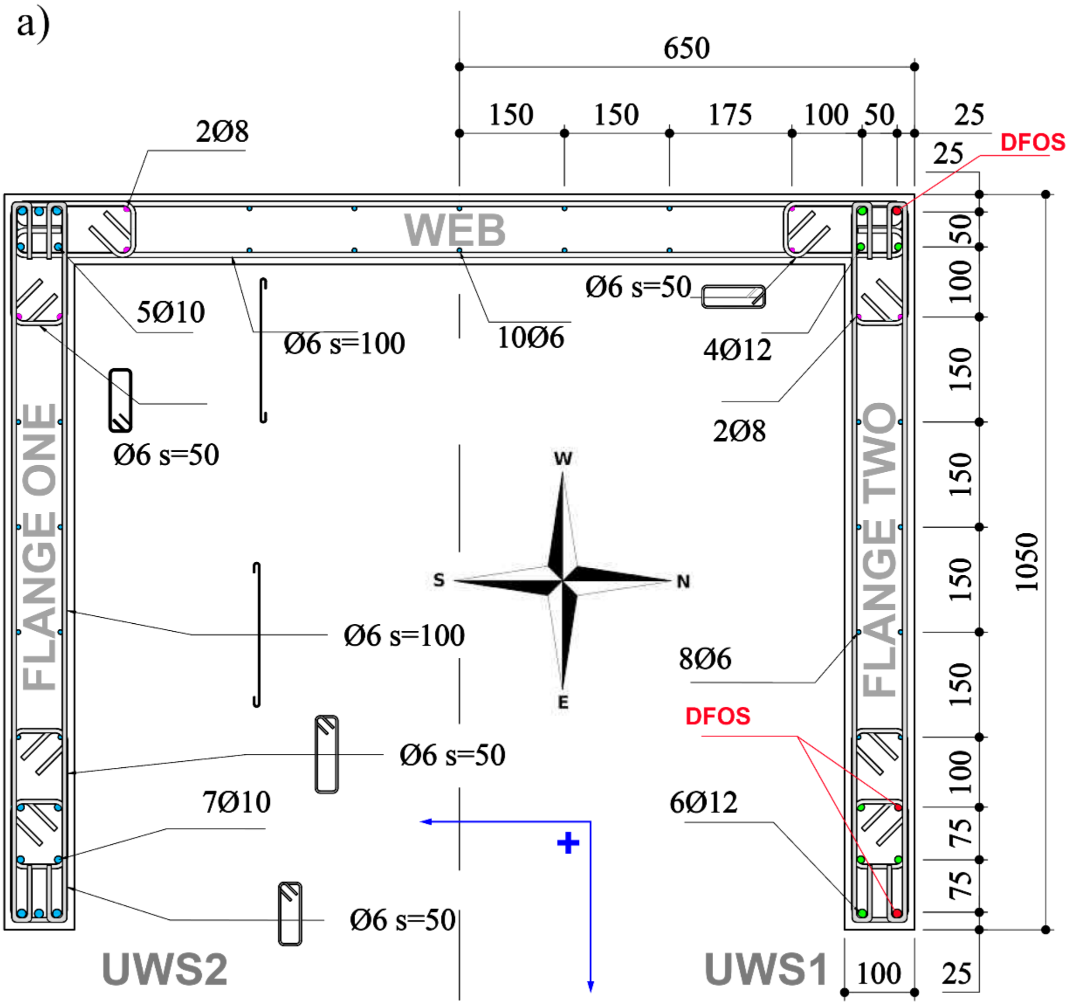

Figure 1 Cross-section, reinforcement layout, and labelling of test units (UWS1 on the right-hand side with indication of DFOS instrumented bars in red, UWS2 on the left-hand side). All dimensions are in millimeters.

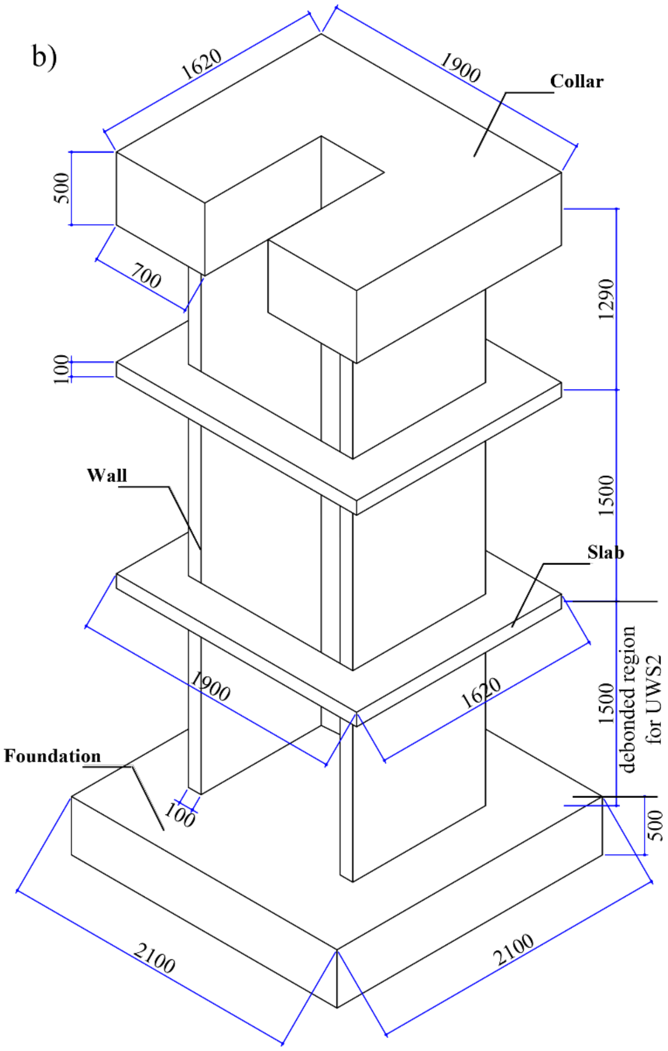

Figure 2 Elevation view of test units UWS1 and UWS2. All dimensions are in millimeters.

MATERIAL PROPERTIES

The design concrete strength for the wall units, defined as the 28-day cylinder strength, was 30 MPa. Table 1 presents the average ("Avg.") and covariance ("COV") compressive strengths (f'_c) of the different wall components, measured from testing 150 mm (diameter) x 300 mm cylinders at 28 days. For each wall component, three cylinders were tested. Note that unit UWS1 was tested 41 days after concrete casting of the wall, while unit UWS2 was tested at 28 days.

Table 1 Mean values of the concrete cylinder compressive strengths.

	Cylinder compressive strength (f'_c, MPa)					
	Foundation		Wall		Collar	
	Avg.	COV	Avg.	COV	Avg.	COV
UWS1	29.6	0.02	27.0	0.52	34.6	1.04
UWS2	24.7	0.24	30.3	0.64	29.5	0.25

Table 2 lists, where applicable, the average ("Avg.") and covariance ("COV") of yield strength (f_y), ultimate strength (f_u), yield strain (ε_{sy}), ultimate strain (ε_{su}), number of bars tested (n), and Young's modulus (E_s) for the different reinforcing materials and longitudinal rebar diameters (d_{bl}). The hardening strain (ε_{sh}), indicating the end of the constant strength yield plateau for steel, is also provided in Table 2. In compliance with the requirements of Eurocode 8 (CEN, 2004b) to ensure ductility and energy dissipation, Class C steel was used for all the longitudinal reinforcing bars in unit UWS1 and the 6 mm-diameter longitudinal bars in unit UWS2. Class C steel was also used for the transverse (shear and confinement) reinforcement in both wall units. Figure 3a shows the stress-strain relationship for the Class C steel with a 12 mm diameter, used for the longitudinal reinforcement at the boundary ends of unit UWS1.

Table 2 Mechanical properties of the reinforcing bars. “Avg.” refers to the average value, whereas “COV” refers to the covariance.

Material	d_{bl}	f_y		f_u		ε_{sy}		ε_{sh}		ε_{su}		E_s		n
-	[mm]	[MPa]		[MPa]		[%]		[%]		[mm/mm]		[GPa]		–
		Avg.	COV	Avg.	COV	Avg.	COV	Avg.	COV	Avg.	COV	Avg.	COV	
Steel	6*	577	53	623	10	0.28	0	–	–	4.6	0.5	208	100	5
Steel	6#	550	2	676	6	0.27	0	–	–	9.5	0.6	207	13	3
Steel	8	538	2	664	0	0.27	0	2.7	0	12.0	0.0	196	112	3
Steel	12	580	9	690	4	0.29	0	2.1	0	10.1	3.2	199	0	3
FeSMA^	10	555	–	830	–	0.35	–	–	–	16.0	–	157	–	1

* transverse steel

longitudinal steel

^ values reported are constrained by the limitations of the testing apparatus

Compared to unit UWS1, the Class C 12 mm steel rebars were replaced by iron-based shape memory alloy (FeSMA) bars, illustrated as blue dots on the left-hand side of Figure 1. Ribbed FeSMA rebars were sourced from the Swiss company re-fer AG (re-fer, 2025) with an alloy composition of Fe-17Mn-5Si-10Cr-4Ni-1 (V,C) (in mass-%). These FeSMA bars were prestrained by the manufacturer to a minimum of 4 % (Shahverdi *et al.*, 2018) to achieve the desired shape memory effect after "activation," allowing them to undergo substantial reversible deformation and recover their original shape. The shape memory effect refers to the FeSMA's ability to return to its pre-deformed shape when exposed to a specific stimulus, such as stress. "Activation" involves applying a stimulus, such as heat, to trigger the recovery of the bars' original shape. When the deformation of the FeSMA is constrained—such as by the encasing concrete—recovery stresses develop in the FeSMA. These stresses are used to effectively apply a prestressing effect to the wall, thus harnessing the shape memory effect of the material. In this study, the goal was to use this prestressing effect to reduce residual displacements in the wall, compared to a conventional steel-reinforced counterpart. Notably, recent tests on RC bridge columns reinforced with the same FeSMA material have shown promising reductions in residual displacement (Raza *et al.*, 2023). All the FeSMA rebars have a diameter of 10.7 mm, and their surface geometry complied with the British Standard 6744:2001 (BSI, 2009). A recent study by Fawaz and Murcia-Delso (2020) involving pull-out tests on the same FeSMA bars found that, in confined specimens—such as the walls examined in this study—the bond stress–slip behavior was comparable to that of conventional steel rebars. However, the average bond strength was approximately 15% lower. The study also showed that activation temperature had only a minor effect on the bond stress–slip response.

The FeSMA rebars underwent heating at a specific activation temperature to achieve the desired recovery stresses. It is noted that the prestrain level before activation, and the activation temperature, are recognized as the two fundamental parameters in terms of the recovery stress of FeSMA. Previous research has shown that the recovery stress of FeSMA reaches a plateau of approximately 350 MPa within the temperature range of 250°C to 300°C (Raza *et al.*, 2023). Additionally, Gu *et al.* (2021) indicated that the recovery stress of FeSMA strips does not increase when the activation temperature exceeds 350 °C. In other research studies, the thermal activation of the FeSMA rebars was performed by gas flame heating (Raza *et al.*, 2023), electric resistive heating (ERH) (Michels *et al.*, 2018; Soroushian *et al.*, 2001), or heating tapes (Vahedi *et al.*, 2024). The second option, thermal activation via ERH, was used in unit UWS2 as it allows for a more precise and uniform temperature application; the latter was monitored by thermocouples. ERH, also known as the Joule effect—where material temperature rises under an electrical current—has been widely used in previous research to activate FeSMA rebars (e.g., Liu *et al.*, 2023; Raza *et al.*, 2022a). In this study, the electrical current was applied directly to the rebars after concrete curing and before the shake table testing.

Different researchers have used varying "holding times," which refer to the interval during which the maximum activation temperature is attained and maintained. For instance, Raza *et al.* (2022b) used a holding time of 30 minutes with a target activation temperature of 160 °C, while Liu *et al.* (2023) recommended a holding time of only 120 seconds.

Laboratory tensile material tests were conducted on the 10.7 mm FeSMA rebar. The activation temperature using ERH in the laboratory exceeded 450 °C, perhaps considerably, as the bar was observed to glow red from the heat. This high temperature value was not intended and can be explained by a malfunctioning of the thermocouple data acquisition system. Figure 3b shows the prestress measured by the universal tensile machine in the laboratory during the first minutes of heat application and after, i.e. during subsequent cooling over a period of almost three hours. The results are consistent with the stress plateau observed in previous tests (Raza *et al.*, 2023). Figure 3a presents in blue the resulting cyclic stress-strain behavior of the previously activated 10.7 mm FeSMA rebar. The corresponding mechanical properties are provided in Table 2, and the limited number of FeSMA bars tested (*n*) is due to the restricted availability of materials. It is worth noting that the tensile testing machine reached its stroke limits while testing the FeSMA bar over an effective gauge length of approximately 625 mm, indicating that higher strength and strain values could likely have been achieved (Figure 3a). According to the mechanical properties from re-fer (2025), these bars have an elongation at break exceeding 20%. Although Figure 3a may not clearly illustrate the recentering capabilities, it is worth noting that the same activated material was used in RC columns (Raza *et al.*, 2023), where it reduced residual drifts by up to 75 % compared to the same specimen reinforced with conventional steel.

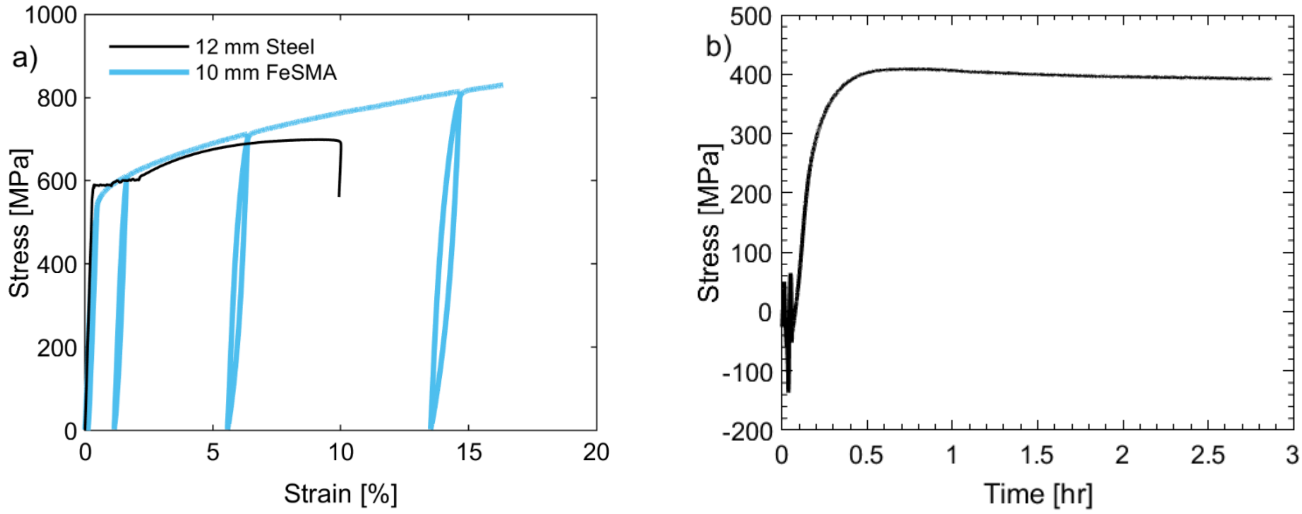

Figure 3 (a) Stress-strain relationship for the class C 12 mm steel reinforcement and the 10.7 mm FeSMA reinforcement (b) prestress achieved for the FeSMA 10.7 mm rebar during initial application of electrical resistive heating, and three-hour cooling phase.

TEST SETUP

The wall units, one of which is shown in Figure 4, were tested on the large shake table at the National Laboratory for Civil Engineering (LNEC) in Lisbon, Portugal. The maximum capacities of the horizontal actuators are 700 kN in the west-east (WE) direction and 500 kN in the north-south (NS) direction. Figure 1 illustrates the orientation of the wall relative to these cardinal directions. The positive axis conventions are defined as north to south and west to east, as indicated in Figure 1. The shake table can achieve maximum displacements and velocities of ±200 mm and ±700 mm/s, respectively, in either direction. The table has a maximum payload capacity of approximately 40 tons.

To generate the required lateral inertial forces and reach the flexural capacity of the scaled wall units, several mass blocks were used. These included 1.13-ton and 0.59-ton blocks, which were connected to the collar (head) of the wall. These mass blocks have a cross-section of 840 mm × 840 mm, with thicknesses of 250 mm for the 1.13-ton blocks (red blocks, Figure 4) and 130 mm for the 0.59-ton blocks (yellow blocks, Figure 4). A total of 16 (arranged in a 4 x 4 grid) 1.13-ton mass blocks were placed on the collar of the wall unit, along with 12 (arranged in a 4 x 3 grid) 0.59-ton mass blocks. This setup results in a total mass of about 25.16 tons above the collar. Including the mass of the wall unit's collar, which is approximately 3.27 tons, the total mass at the top of the wall is 28.43 tons.

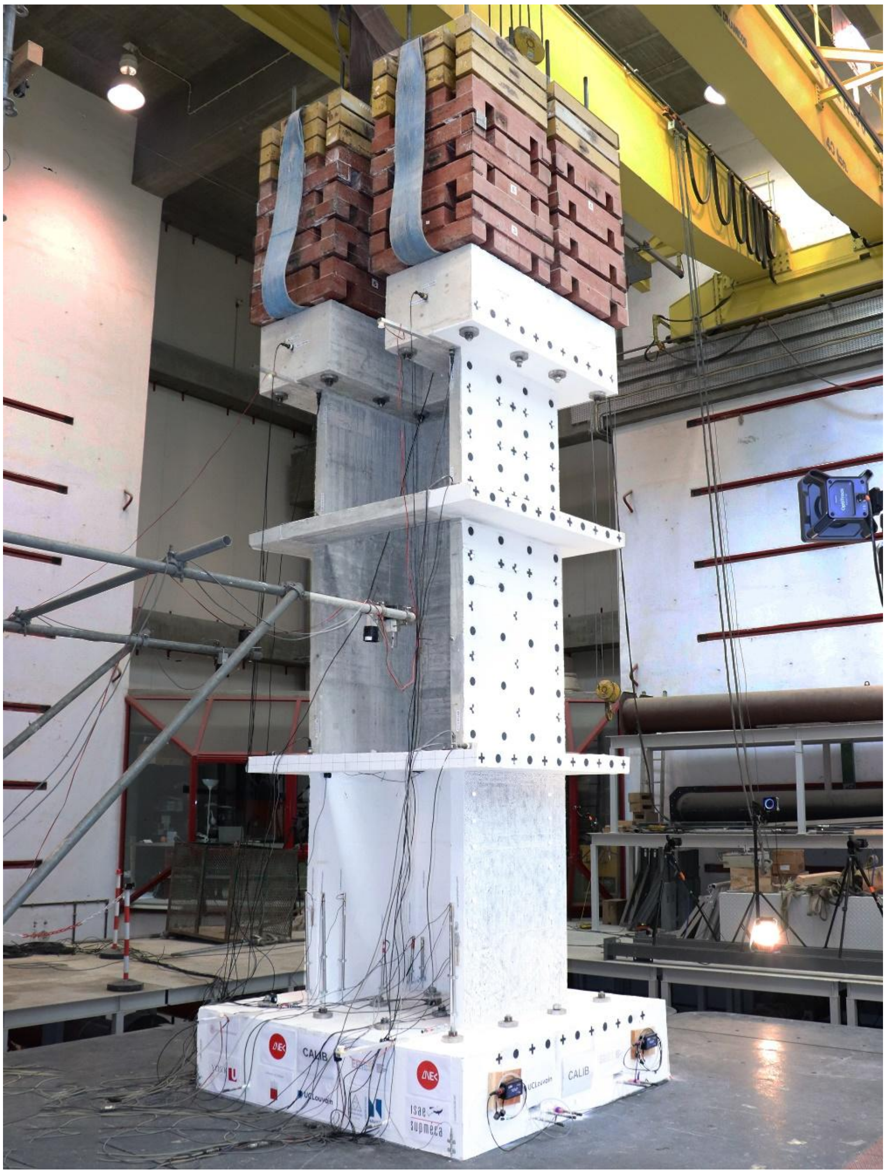

Figure 4 Photo of test unit UWS2 taken from the north-east prior to testing.

INSTRUMENTATION

Conventional Instrumentation

Throughout testing, the behavior of the walls was monitored using conventional instrumentation. Linear variable differential transformers (LVDTs) measured the vertical elongation of the wall edges and the wall base with a gauge length of 70 mm. LVDTs also measured any uplift of the foundation edges. Wire potentiometers (also referred to as string pots) were used to measure the global in-plane horizontal displacements at the collar (head) of the wall and the shear deformation of the lower region of the wall. Additionally, an optical measurement system was used to measure the in-plane displacements at the collar and base of the wall. Accelerometers were installed at the base (on the foundation), the intermediate slabs, and the collar of the wall to measure the in-plane and vertical accelerations. For the sake of brevity, the precise locations of these instruments, along with their corresponding names and numbers, are not included here but can be found in the dataset (see the *Organization of Test Data* section).

Virtual Targets and DIC

The motion of the Web and Flange Two (see Figure 1) was recorded during both experimental campaigns (UWS1 and UWS2) using a network of cameras synchronized by an external electronic trigger. The trigger generates a Transistor–Transistor Logic (TTL) signal that synchronizes all cameras and the data acquisition (DAQ) systems of the conventional sensors. This setup ensures that the timestamps of the recorded images are aligned with other collected data.

Two different surface texturing and camera systems were applied to the structure to facilitate optical measurements. As shown in Figure 5b, the first texturing involved a grid of 168 (UWS1) and 201 (UWS2) black spray-painted circles and crosses, each approximately 5 cm in diameter. Such virtual sensor targets were painted on specific locations of the wall units — such as the base, slabs, collar, and second and third levels (Figure 5a) — to capture the global dynamic behavior of the RC U-shaped walls, including modal identification and maximum amplitudes (Lo Feudo *et al.*, 2025). Discrete target detection and tracking through digital image correlation enabled the determination of each target's spatial position at every frame, recorded at a frequency of 100 Hz. Additionally, the use of cruciform (cross-shaped) virtual sensors theoretically allow for the measurement of not only translational motions, as provided by the circular targets, but also of local rotations at the sensor locations; this is an ongoing work. Future studies will further investigate the rotational behavior of these virtual sensors caused by wall flexure.

Three Basler digital cameras — two acA1300-200um models and one acA1440-220um model — were used to record the upper regions of the walls above the ground floor. These cameras captured the motion of the virtual sensors, with frames acquired in real-time using Pylon Viewer software and transmitted to three computers via Micro USB 3.0 connections. To enable three-dimensional (3-D) reconstruction of the vibratory field based on stereovision principles, the cameras were strategically positioned. Specifically, one camera captured the exterior surface of the Web, another focused on the exterior surface of Flange Two, and the third camera recorded both surfaces, ensuring comprehensive coverage. More details can be found in the paper by Lo Feudo *et al.* (2025).

The second surface texturing involved the application of a speckle pattern to the ground floor surfaces of the Web and Flange Two, designed to enable high-resolution measurements of displacement and strain fields, as well as the evolution of crack patterns. As illustrated in Figure 5c, this speckle pattern was created using a stamp roller to produce a random distribution of black dots, each approximately 2.5 mm in diameter.

To capture data, three-dimensional digital image correlation (DIC) systems were employed. Each system consisted of two pairs of video cameras, with one pair monitoring the Web and the other pair focusing on Flange Two. Specifically, two Vieworks VC-12MX-M-180 cameras (designated as V1 and V2) recorded the motion of the Web, while two JAI SP-12000M-CXP4 cameras (designated as JA1 and JA2) captured the motion of Flange Two. The DIC system recorded at a frequency of 100 Hz and 50 Hz for units UWS1 and UWS2, respectively. Detailed information regarding the camera equipment and settings can be found in the documentation accompanying the dataset.

It is important to note that, to manage data volume, only the ground motion (GM) runs were recorded during the UWS1 campaign. In contrast, for the UWS2 campaign, noise sequences (used for modal identification between GM runs) were also recorded by the Basler cameras for the virtual targets, specifically in the EW direction.

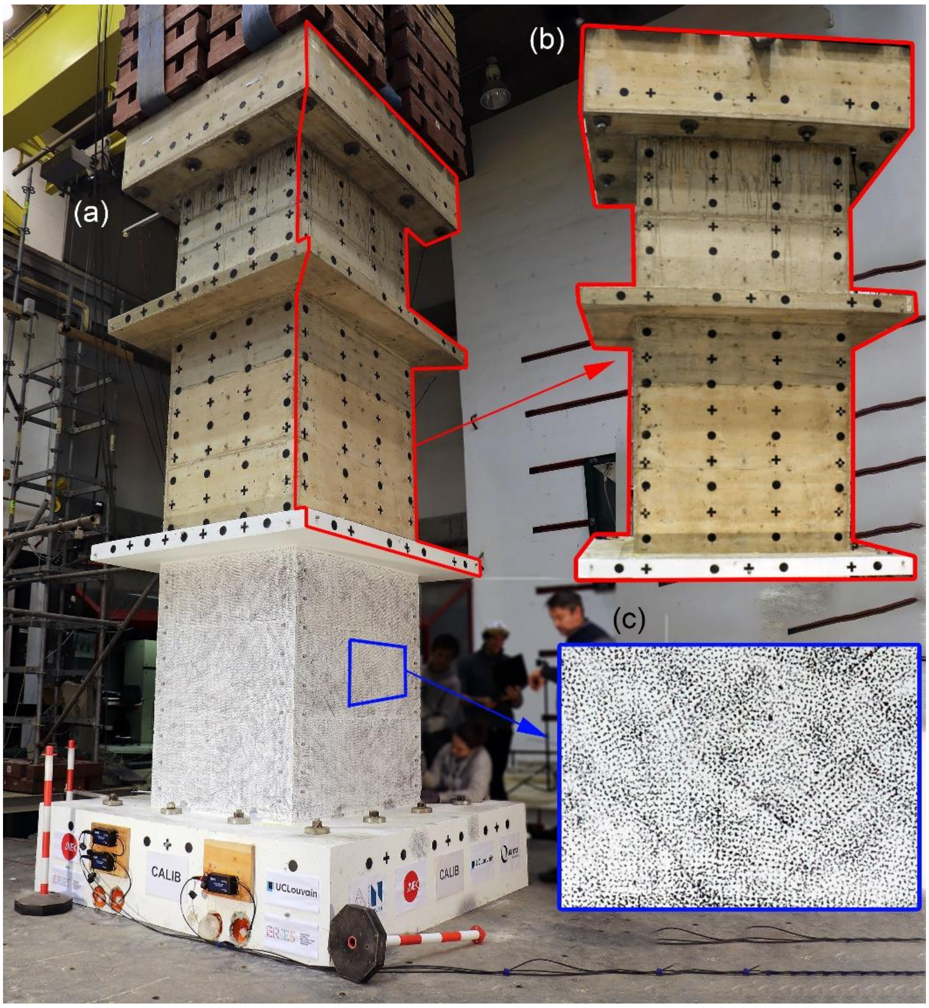

Figure 5 Surface texturing for optical measurements (a) photo of the wall taken pre-test from the north-west (facing south-east) of the Web and Flange Two (b) circle and cross targets to capture global response (c) speckle pattern for high-resolution strain and displacement field of the first (ground) floor.

Motion Capture

The OptiTrack motion capture system used in the tests consists of ten cameras: four OptiTrack Prime^X 22 cameras (2.2 MP resolution, 2048 × 1088) and six OptiTrack Prime 17W cameras (1.7 MP resolution, 1664 × 1088). The cameras were strategically positioned around the test specimens, primarily towards the northwest, to capture multiple viewpoints (both in height and orientation) of the exterior surfaces of the north flange (or Flange Two, in Figure 1) and web. All cameras operated at a frame rate of 100 Hz with an exposure time of 8 ms. Motive software (version 3.0.3) was used to track the three-dimensional displacements of 90 reflective markers (19 mm in diameter) affixed to the wall's exterior surface.

Before measurement recording, the system underwent a calibration phase using a CW-500 calibration wand, which contains three precisely spaced markers. The wand was moved within the cameras' field of view to determine each camera's position, orientation, and any image distortions. This process generated a 3D capture volume within Motive. Calibration accuracy was assessed using two error metrics: (i) mean ray error, which measures how precisely the tracked rays from each camera converge on a 3D point; (ii) mean wand error, which represents the difference between the detected and expected wand length. For the tests presented herein, the mean ray error was 0.8 mm, and the mean wand error was 0.13 mm—both indicating high calibration accuracy. Finally, a CS-400 calibration square was used to align the ground plane with the shaking table.

Lo Feudo *et al.* (2025) shows a detailed comparison between the 3D optical tracking of the painted targets, motion capture markers, and conventional instrumentation employed in this study.

Distributed Fiber-Optic Strain Sensing

State-of-the-art high-definition fiber-optic sensing was employed to measure strains in selected reinforcing bars indicated in Figure 1 for UWS1. This instrumentation technique has been successfully applied in previous quasi-static testing of RC U-shaped core walls using the same methodology (Hoult *et al.*, 2023b). Strain data was collected using the LUNA ODiSI 6104 Series optical distributed sensor interrogator, a four-channel system from DIMIONE Systems. The DFOS provided high-spatial-resolution measurements (5.2 mm) with an accuracy of more than 30 με. Data was recorded at a frequency of 16.67 Hz during the testing of unit UWS1.

Three longitudinal rebars in the north flange of wall unit UWS1 were selected for bonding DFOS to the reinforcing steel to derive strain profiles along the height of the wall. A small groove (1 mm wide and 1 mm deep) was cut along the longitudinal ribs of each rebar, a widely adopted practice in previous research to securely attach DFOS to steel reinforcement and to minimize the risk of premature fiber failure (Bado *et al.*, 2020; Hoult *et al.*, 2023a; Michou *et al.*, 2015; Quiertant *et al.*, 2012; Zhang *et al.*, 2021). The sensing fiber used was a polyimide-coated fiber. Following preliminary performance tests, a general-purpose adhesive (“Loctite 401,” based on cyanoacrylate technology) was applied to bond the fiber within the groove, a method that has been successfully implemented in previous studies (Barrias *et al.*, 2018; Berrocal *et al.*, 2021; Hoult *et al.*, 2023a). Additionally, an epoxy coating (“ESK-50”) was applied over the glued fiber to provide an extra layer of protection between the fiber and the surrounding concrete. A more detailed explanation of the instrumentation setup is provided by some of the authors in Hoult *et al.* (2023a).

Unlike previous quasi-static tests where this instrumentation technique was successfully employed (e.g., Hoult *et al.*, 2023b), the dynamic nature of the tests reported here resulted in significant data loss from the LUNA system during recording. According to post-test communication with Luna Innovations (personal communication, June 14, 2024), the ODiSI system is primarily designed for quasi-static testing, and its performance is compromised under dynamic conditions, particularly due to slower measurement rates, longer sensor lengths, higher excitation frequencies, and large strain amplitudes. Despite these challenges, some strain data was captured, especially during the initial input motion levels, albeit sporadically. As a result, the authors have chosen to publish the raw DFOS data in its current form, recognizing its potential value for future research.

Crack widths, photos, and videos

Photos of all wall faces of each of the test units were taken after every ground motion (GM), along with closer-range photos focusing on any notable local damage (e.g., cracks, concrete spalling, splitting, crushing, rebar buckling, and fracture). Additionally, several cameras, including GoPros, were used to capture time-lapse recordings and standalone videos of both wall units. These resources have proven to be very powerful and useful in the post-analysis of the wall behavior, contributing to a better understanding of the progression of damage in each of the wall units investigated.

SIMILITUDE, GROUND MOTIONS, AND LOADING PROTOCOL

Similitude Laws

As explained in Pinho (2000), reproducing the true dynamic response of a prototype core wall structure requires accurate simulation of the geometry, initial and boundary conditions, stress-strain relationship of the materials, and mass and gravity forces. The latter poses a challenging problem, where the simulation of the mass and gravity forces are closely linked to the similitude law adopted. As such, the Cauchy-Froude law must be respected in the dynamic testing of scaled models (Pinho, 2000). Assuming that the materials are the same for the full-scale prototype and half-scale model, the scale factors using the Cauchy-Froude similitude laws can be derived. It is worth noting that, because the density of the concrete and reinforcing steel materials becomes inversely proportional to the geometric scale factor (λ = 2 in this case), it is not uncommon for the scale of the specific mass to be considered independently of the geometric scale. As previously mentioned, the total applied mass used for these tests is 25.16 ton, which, in conjunction with the self-weight of the unit (estimated at 12.95 ton, assuming a conservative reinforced concrete density of 2500 kg/m^3), is below the maximum payload of the shake table, of 40 ton. Importantly, these similitude laws and the corresponding scaling factor/s were applied to the ground motions discussed in the next section, which essentially shifts the spectral acceleration response.

Loading Protocol

The 2016 Central Italy earthquake sequence caused significant damage and loss of life (Sextos *et al.*, 2018), representing the largest Italian seismic sequence densely observed with modern geodetic measurements (Cheloni *et al.*, 2017). The moment magnitude M_w 6.5 event was the largest of the three main events that occurred on 30 October 2016. The normal faulting event ruptured a 15 km-long section of the fault at a shallow depth of 3–7 km (Cheloni *et al.*, 2017; Stewart *et al.*, 2018). The seismometer station MZ04 was one of many that captured the event of October 30. The MZ04 recording station (Luzi *et al.*, 2020) was located at a close Joyner-Boore distance (R_{jb}) of 6.4 km, with an epicentral distance of 23 km. The station is situated on site class C (CEN, 2004b) with an estimated shear wave velocity in the upper 30 m (V_{S30}) measured of 355 m/s. The 5 % damped pseudo spectral accelerations (PSa) response captured by the MZ04 station are given in Figure 6a. These spectra were adjusted using a time-step (dt) correction from 0.005 s to 0.0035 s, following the laws of similitude (Candeias *et al.*, 2023) (see also the previous section). Specifically, the ground motions were time-scaled by a factor of $1/\sqrt{\lambda}$ (where λ is geometric scaling factor), resampled to 200 Hz (dt = 0.005s), and cropped to a 30-second duration, with a 40 Hz low-pass filter applied. The peak ground acceleration (PGA) in the north-south (NS) and west-east (WE) directions is approximately 0.64 g and 0.81 g, respectively.

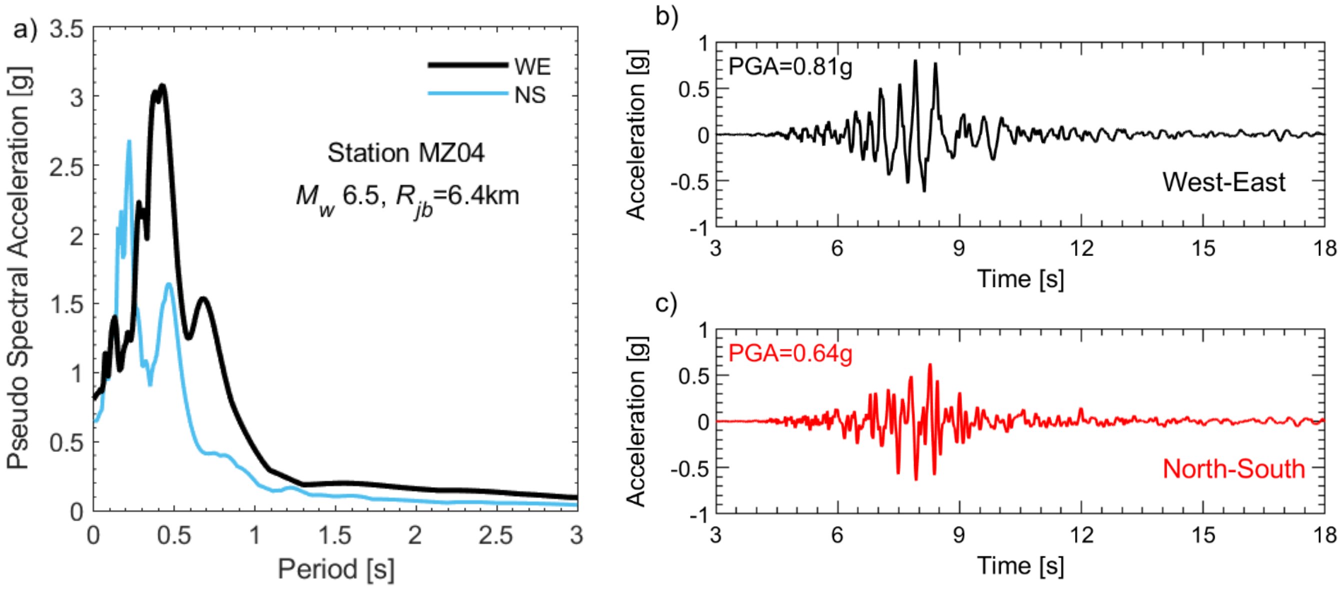

Figure 6 Moment magnitude M_w 6.5 event from the 2016 Central Italy earthquake sequence on 30 October: (a) 5 % damped pseudo spectral acceleration (corrected using a scaled time-step) (b) acceleration-time history in the west-east (i.e., HNN) (c) acceleration-time history in the north-south (i.e., HNE).

The dynamic tests of units UWS1 and UWS2 included nine different levels of ground (input) motion (GM0 – GM8), each corresponding to a different scale combination of the horizontal west-east (HNN record in the MZ04 station) and north-south (HNE record in the MZ04 station) components. The HNN ground motions were applied in the WE direction of the shake table, and the HNE ground motions were applied in the NS direction. As previously defined, the positive direction of the ground motion corresponds to the positive direction of the shake table (see Figure 1).

For consistency with the shake table cardinal directions and conventions, the HNN and HNE directions have been renamed WE and NS, respectively. Table 3 shows the combined scaling factors applied to each of the WE and NS input motions for each run (i.e., GM0 – GM8). The first input motion, GM0, and all odd-numbered input motions (e.g., GM1, GM3, etc.), are unidirectional in the WE direction only. The other input motion levels are bidirectional and are intended to induce bi-directional flexural and torsional demands.

Table 3 Scale factors (in percent) used for the input motions captured by MZ04 of the M_w 6.5 Central Italy earthquake event.

	Scale [%]	
	HNN (west-east on shake table)	HNE (north-south on shake table)
GM0	10	0
GM1	25	0
GM2	25	25
GM3	50	0
GM4	50	50
GM5	75	0

GM6	75	75
GM7	100	0
GM8	100	100

As noted in the *Material Properties* section, the FeSMA rebars in unit UWS2 required heating for activation and to induce the desired shape memory effect upon cooling, thereby prestressing the wall. A 15 kW power supply, originally designed for welding, was repurposed for Electrical Resistive Heating (ERH) of the FeSMA bars. Several thermocouples were attached to some of the embedded rebars to monitor the heating process, targeting a temperature of 250 °C.

To isolate the FeSMA rebars from the surrounding steel reinforcement (e.g., confinement, shear, longitudinal reinforcement, and foundation elements), the bars were primarily wrapped in plastic heat shrink. However, a later inspection of construction photos revealed that some FeSMA bars were in contact with steel reinforcement near the lap splice region above the first intermediate slab. This unintended contact resulted in inconsistent heating, as the ERH system lacked sufficient power to effectively heat the rebars when they were not fully isolated.

The maximum recorded temperatures from thermocouples at each wall corner were: south-east: 399.2 °C, south-west: 63.5 °C, north-west: 98.1 °C, and north-east: 97.8 °C. These temperature readings indicate that the ERH system was largely ineffective. Based on a previously established relationship between activation temperature and induced prestress (Hoult & Almeida, 2024c), the corresponding estimated prestress levels were: 393 MPa, 144 MPa, 203 MPa, and 202 MPa, respectively. Some indirect signs of heat transfer were observed—such as the concrete surfaces at the south-east flange boundary and the north-west web-flange intersection becoming warm to the touch during heating. However, the duration and localized nature of the heat application appeared insufficient to cause any noticeable signs of degradation of the concrete.

Ultimately, the authors conclude that only partial precompression was achieved due to the inconsistent activation of the FeSMA rebars. This uneven heating likely contributed to the observed torsional rotation and increased displacement demand in the northward direction (see "Example Plots of Global Behavior" for further discussion). Additional details on the activation of the FeSMA bars and the corresponding performance of unit UWS2 can be found in the literature (e.g., Almeida & Hoult, 2025).

TEST OBSERVATIONS

This section summarizes some important findings from the tests. Detailed observations of each test for UWS1 and UWS2 are provided in the subsequent sub-sections. At the time of writing this document, the post-processing of some of the experimental data is ongoing. Therefore, the following observations are based on some preliminarily analyzed results and on the observed cracking from visual inspection of the unit after it came to rest following each ground motion (GM). The description of the cracking refers to residual cracking after each test run; the full identification of the crack pattern attained during each input motion, along with the maximum crack opening, will only be available after the post-processing of digital image correlation.

To provide context when comparing engineering parameters such as drift ratio demands, Table 4 presents 5 % damped pseudo spectral acceleration values (in units of g) for both wall specimens across all ground motions. For simplicity, these values were calculated based on the structure's fundamental period, $S_a(T_1)$, determined from the 'noise' sequences used for modal identification before GM0.

Table 4 Pseudo spectral acceleration (5 % damping) corresponding to the fundamental (first natural) period $S_a(T_1)$ for UWS1 (T_1=0.33 s) and UWS2 (T_1=0.32 s)

	$S_a(T_1)$ [g]	
	UWS1	UWS2
GM0	0.15	0.18
GM1	0.65	0.78
GM2	0.68	0.92
GM3	1.07	1.24
GM4	1.08	1.18
GM5	1.52	1.57
GM6	1.55	1.62
GM7	1.90	2.05
GM8	1.99	2.23

Unit UWS1

The initial input motions induced minor hairline cracking on the web's external surface and at the extremities of the flange boundary. GM2, the first series of accelerations applied in both the west-east and north-south directions, led to crack appearance along the wall-foundation interface. Subsequently, the uniaxial input motion GM5 generated a maximum west-east drift ratio (δ_{WE}) of 1.74 %. The drift ratios were calculated by averaging the readings from two potentiometers positioned 4.29 m above the foundation on the eastern face of the collar (head), to the north and south, dividing by the height (of 4.29 m), and subtracting the displacement of the shake table. These two potentiometers were also used to measure the rotations, as indicated below. This level of loading from GM5 caused flexural cracks to develop within the bottom story height (i.e., below the slab) at the flange boundary extremities, exacerbating existing cracks at the wall-foundation interface, which were apparent even after the unit came to rest.

The bi-directional input motions of GM6 induced noticeable torsion, as expected, in combination with flexural actions, likely due to the offset of the shear center of the wall specimen (Hoult, 2021; Hoult & Almeida, 2024a; Hoult & Beyer, 2020). Concrete crushing was observed during GM6 in the corner of the flange-web south-west intersection. During this input motion, the maximum west-east drift ratio (δ_{WE}), north-south drift ratio (δ_{NS}), and torsional rotation (θ_{max}), were recorded to be 1.65 %, 0.65 %, and 25.4 mrad, respectively. Some horizontal sliding at the wall-foundation interface was also visually observed during the shaking on the north flange face along the west-east direction, parallel to the flanges.

Further concrete crushing occurred during GM7 in the south flange (i.e., Flange One) boundary end, and at the flange-web intersection in both the north-west and south-west corners. During GM7, the largest recorded in-plane west-east drift, reaching δ_{WE} = 2.71 %, was observed. Subsequently, the largest amplitudes of bi-directional accelerations with GM8 caused significant crushing in both flange boundary ends. The large attained maximum drifts of δ_{WE} = 1.82 %, δ_{NS} = 0.46 %, and rotation θ_{max} = 27.4 mrad from GM8 also resulted in noticeable buckling of the longitudinal rebars in the south-east flange boundary end – see Figure 7a. Upon inspection, a larger-than-prescribed spacing between two consecutive confining rebars in the south-east flange boundary end was observed, facilitating the aforementioned rebar buckling response. In the east extremity of the north flange (e.g., Flange Two), however, the tight confining reinforcement led to high compressive strain demands, inducing noticeable local out-of-plane buckling of the flange towards the inside of the core wall – see Figure 7b. The residual cracking distributions observed on the outside surface of Flange One after GM8 are depicted in Figure 8a.

Videos of the test during GM8 confirmed suspicions of exacerbated horizontal sliding at the wall-foundation interface in the west-east direction (see Figure 1 for cardinal directions). The preliminary analysis of the Optitrack motion capture system showed a maximum base sliding displacement of 6.7 mm and 7.9 mm during GM7 and GM8, respectively.

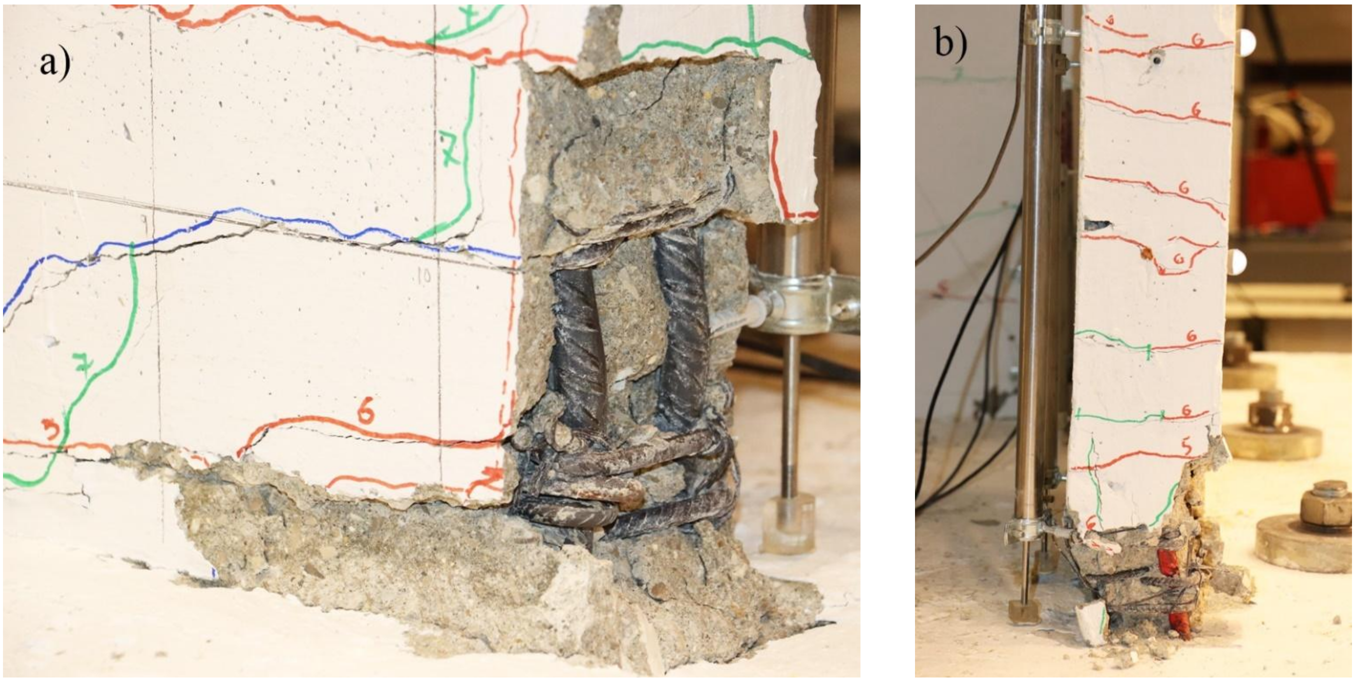

Figure 7 Failure locations of unit UWS1 at the base after GM8 (a) boundary end of Flange One with rebar buckling (b) boundary end of Flange Two with local out-of-plane buckling towards the inside of the wall.

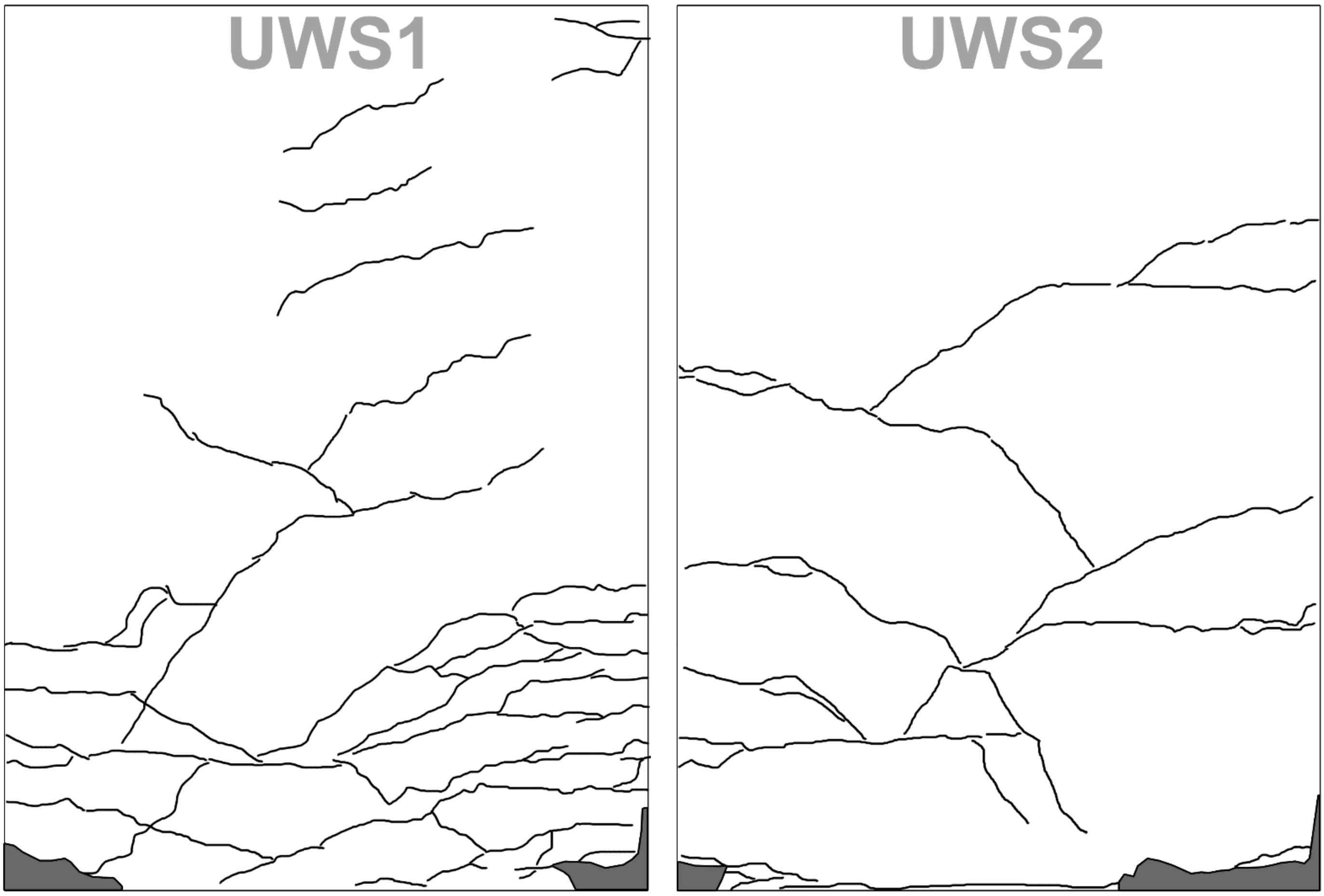

Figure 8 Cracking distribution observed on the outside surface of Flange One after GM8 (a) UWS1 (b) UWS2. The grey-colored regions indicate areas of the wall where the concrete crushed.

Unit UWS2

Similar to the first wall unit (UWS1), the second unit (UWS2) exhibited minor hairline cracking during the initial input motion stages. In particular, vertical splitting cracks developed at the base of the north and south flange boundary ends after GM1, likely due to a combination of horizontal flexural cracking followed by crushing of the unconfined concrete cover. As observed in UWS1, cracks also formed along the wall-foundation interface after GM2. However, unlike UWS1, which experienced flexural cracks near its base under these initial input motions, UWS2 developed near-horizontal flexural cracks approximately 500 mm above the foundation—most notably on the outside surface of Flange One (Figure 8b).

The cracks in UWS2 worsened under GM5 (i.e., 75 % uniaxial west-east loading), which induced a maximum west-east drift (δ_{WE}) of 1.73 %—almost identical to UWS1 under similar spectral acceleration demands (see Table 4). However, unlike UWS1, this level of loading caused the unconfined concrete cover at the flange boundary ends of UWS2 to crush.

Under bi-directional input motions from GM6 (75 % west-east and north-south), additional flexural cracks formed on the inner surfaces of the wall and the outer south face of Flange One. Compared to UWS1, the spacing between these cracks was noticeably larger (Figure 8b), likely due to (partial) debonding of the FeSMA rebars and the minor pre-compression applied through temperature inducement. Interestingly, under these input motions, UWS2 experienced less north-south displacement and rotation than UWS1. The recorded maximum values for west-east drift (δ_{WE}), north-south drift (δ_{NS}), and rotation (θ_{max}) were 1.80 %, 0.39 %, and 15.8 mrad, respectively. Furthermore, UWS2 exhibited minimal horizontal sliding, differing from the behavior observed in UWS1.

Further concrete crushing at both flange boundary ends was observed during GM7, exposing the longitudinal FeSMA bars (encased in two layers of plastic heat shrink, to promote debonding as discussed above, and guarantee electrical insulation) in these regions (Figure 9). During GM7, UWS2 reached its highest recorded in-plane west-east drift (δ_{WE} = 2.39 %), which was approximately 13 % lower than that of UWS1, despite the slightly lower spectral acceleration demands (see Table 4). As with UWS1, the subsequent bi-directional accelerations of GM8 caused severe crushing of the north-east flange boundary end (Figure 8). The attained maximum drifts of δ_{WE} = 1.97 % and δ_{NS} = 0.56 %, along with a rotation of θ_{max} = 24.8 mrad, also led to noticeable buckling of the longitudinal rebars in this boundary end (Figure 8), even with the closely spaced transverse hooks (confinement) at 50 mm. The buckling behavior observed in UWS2 was consistent with the trends seen in UWS1.

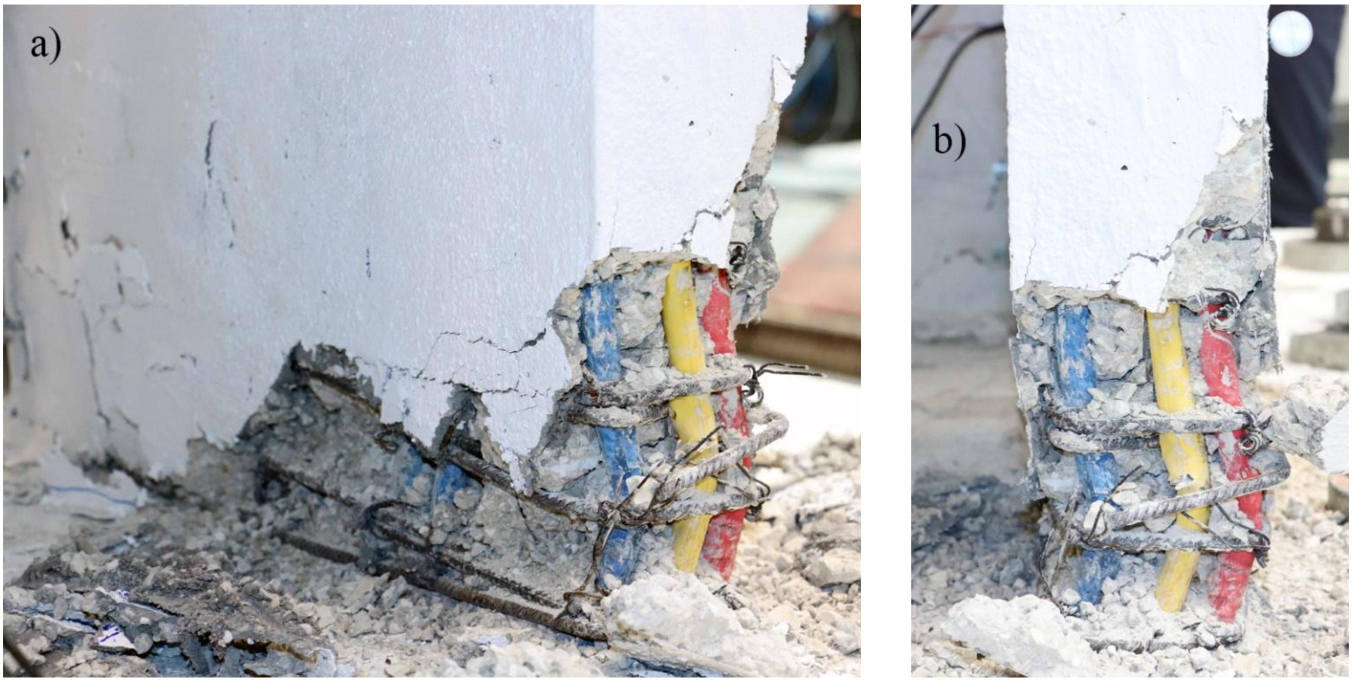

Figure 9 Failure locations of unit UWS2 at the base of Flange Two after GM8. The longitudinal rebars were wrapped in colored heat shrink plastic for the purpose of electrical insulation with the rebar cage, and to promote debonding.

ORGANIZATION OF TEST DATA

All test data for UWS1 and UWS2 are publicly available for download from *Dataverse* at https://doi.org/10.14428/DVN/MSDSWS. The data folder structure is summarized in Figure 10 and can also be viewed directly on *Dataverse* by selecting the "Tree" view. The dataset is organized by specimen, with dedicated folders for each test unit, labeled "UWS(i)".

Before proceeding, it is important to note that Dataverse automatically converts certain file types, such as Microsoft Excel (.xlsx) and comma-separated values (.csv) files, into tabular data (.tab) format for online viewing. However, users have the option to download the original uploaded files in their native formats, as described below.

UWS(i) FOLDERS

The data is organized by wall unit. Figure 10 illustrates the folder and file structure for a generic specimen, UWS(i) ("i" stands for 1 or 2), representing the standardized layout. However, minor variations exist between the two wall units due to differences in instrumentation and test setup. Each wall unit dataset contains two main folders:

1. "UWS(i)_General". This folder contains the following files:
    - "UWS(i)_Lab_Book.xlsx": a copy of the laboratory notebook, which records all of the observations made during the experimental tests, is provided in the form of a Microsoft Excel spreadsheet.

- "UWS(i)_Specimen_Description.pdf": a report summarizing the test specimen and test setup.
- "UWS(i)_Plans.pdf": the wall construction drawings, with detailed representation of the reinforcement layout.
- "UWS(i)_Test_Report.pdf": a test report summarizing the observed behavior and overall test results.

There are also additional sub-folders:

(i). "Material_Tests": this sub-folder contains the results of the material tests that were performed on the concrete (i.e., compression tests on regular 150 mm × 300 mm cylinders).

(ii). "Photos": this sub-folder contains the collected photos before and during the test, taken at subsequent load stages, and separated by the photo of the "GM" (i.e., Ground Motion) number sign attached to the wall units.

(iii). "Videos": this sub-folder contains videos captured by cameras, such as the Go Pros, at various locations during testing.

2. "Processed_Data". In general, this folder contains different processed data files in Binary MATLAB (.mat) (Mathworks, 2020), Comma Separated Values (.csv), and Microsoft Excel (.xlsx) formats. The following files can be found in this sub-folder:
   - "UW(i)_Processed_Data.pdf": a document that provides more detailed information on the processed instrumentation files. This important document summarizes all the data acquisition files and how they can be read.

   Sub-folders at this sub-level contain different processed data:

   (i). "Conventional": this sub-folder contains the processed dataset from the conventional instrumentation (e.g., potentiometers, LVDTs, accelerometers, etc). This data is stored in a Microsoft Excel file, "UWS(i)_DATA.xlsx". The Microsoft Excel file contains nine tabs, corresponding to each ground (input) motion intensity (i.e., GM0 through to GM8). Furthermore, each column of data corresponds to an instrument that can be visualized in the "Instrumentation_Setup.pdf" file, also stored in this sub-folder. For more information on how to use this data, please see the "UW(i)_Processed_Data.pdf" document.

   (ii). "DFOS" (only applicable to unit UWS1): this sub-folder contains the processed and indexed strain measurements captured by the DFOS system; these files are only provided in Binary MATLAB (.mat) file type. Two files are included in this sub-folder:
   - "UW(i)_OpFib_Parameters.mat" contains instrument information about the distributed fiber optic sensors (e.g., frequency, location of gages, recording time, etc).
   - "UW(i)_OpFib_Strain.mat" contains the strain measurements (in units of microstrain = $\times 10^{-6}$ mm/mm) recorded during testing.

(iii). "OptiTrack": this sub-folder contains data from the motion capture OptiTrack instrumentation. This data is separated into files corresponding to each ground motion (GM) and is provided in Comma Separated Value (.csv) files. Each column of the .csv files contain information on the x-, y-, and z- coordinates of the different markers. More information on how this file can be interpreted can be found in the "UW(i)_Processed_Data.pdf" document.

(iv). "Virtual_Targets": this sub-folder contains the data corresponding to the optical measurements extracted from the circular and cross virtual targets painted on the surface of the walls. Similar to the OptiTrack data, Comma Separated Value (.csv) files are provided for each ground motion intensity, and each column of data contain information on the x-, y-, and z- coordinates of the virtual targets. More information on how this file can be interpreted can be found in the "UW(i)_Processed_Data.pdf" document.

(v). "DIC": this sub-folder contains exported, processed digital image correlation (DIC) results. Due to the large size of the full dataset, only selected displacement and strain fields have been included. Specifically, the data corresponds to the outside surfaces of the Web and Flange Two at the largest north-south and east-west global wall displacements, respectively, for each ground motion run. Further details on interpreting this file can be found in the UW(i)_Processed_Data.pdf document. Please note that, at the time of writing, the DIC data for both wall units has not yet been fully processed or compiled. It is expected to be uploaded to the dataset in late 2025.

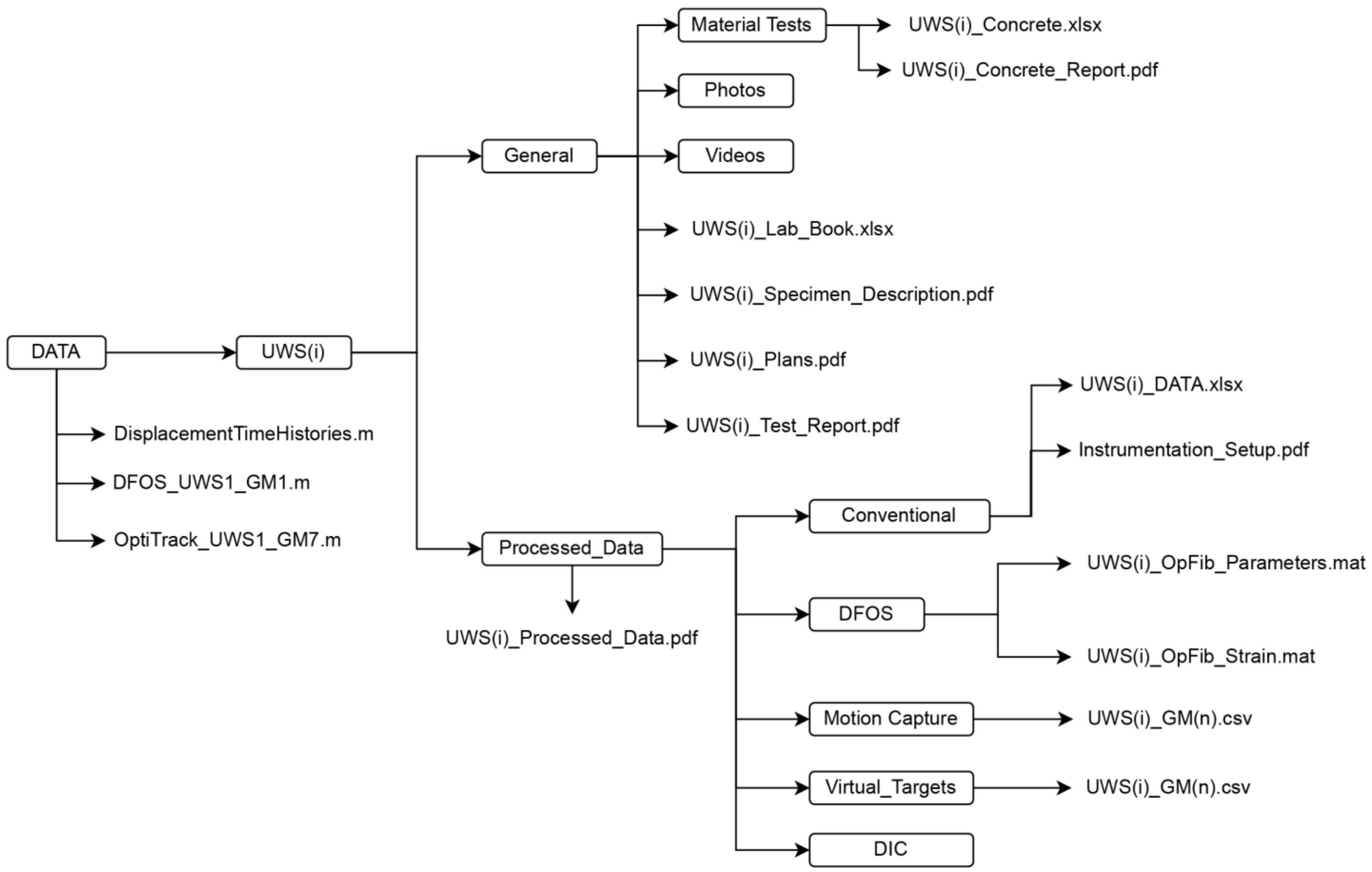

Figure 10 Flowchart of test data organization. The *i* and *n* parameters correspond to the wall unit number (1 or 2) and the ground motion number (0–8), respectively.

POSTPROCESSED DATA AND EXAMPLE PLOTS

This section includes some examples of plots and figures that can be produced by using the provided experimental data. All plots have been created using the post-processed data. MATLAB files (".m") have been provided on the online repository that can replicate the plots and figures in this section (see Figure 10, under "DATA").

EXAMPLE PLOTS OF GLOBAL BEHAVIOUR

Figure 11 shows the displacement time histories for both test units, UWS1 and UWS2, under each ground motion (GM), excluding GM0. West–east displacement ("WE Disp.") was calculated as the average of two string potentiometers (SP10 and SP11) mounted at the flange ends of the collar, 4290 mm above the foundation. North–south displacement ("NS Disp.") was measured using SP7, located on the north side of the collar, 4290 mm above the foundation, near the wall web. In both directions, the reported displacements are relative, obtained by subtracting the displacement of the shake table.

For unidirectional input motions in the west-east direction (GM1, GM3, GM5, and GM7), the corresponding west-east displacement of both test units is nearly identical, despite differences in reinforcement type and content (i.e., steel vs. FeSMA). However, under bidirectional input motions (GM2, GM4, GM6, and GM8), a noticeable difference emerges in the north-south displacement between the two test units.

For instance, under GM8, UWS1 exhibits a displacement of -19.9 mm (i.e., toward the north), whereas UWS2 records -24.1 mm. This distinction is significant because UWS2 also experienced greater crushing at the north flange boundary end. It is likely that the increased displacement demand in the northward direction, coupled with displacements to the east and a rise in torsional rotation, contributed to the extent of crushing in UWS2 compared to UWS1 (see Figure 7b vs. Figure 9).

These figures can be reproduced using the "DisplacementTimeHistories.m" MATLAB script, located in the primary DATA folder (see Figure 10). The data files used to generate these plots can be found in DATA / UWS(i) / Processed_Data / Conventional / DATA.xlsx.

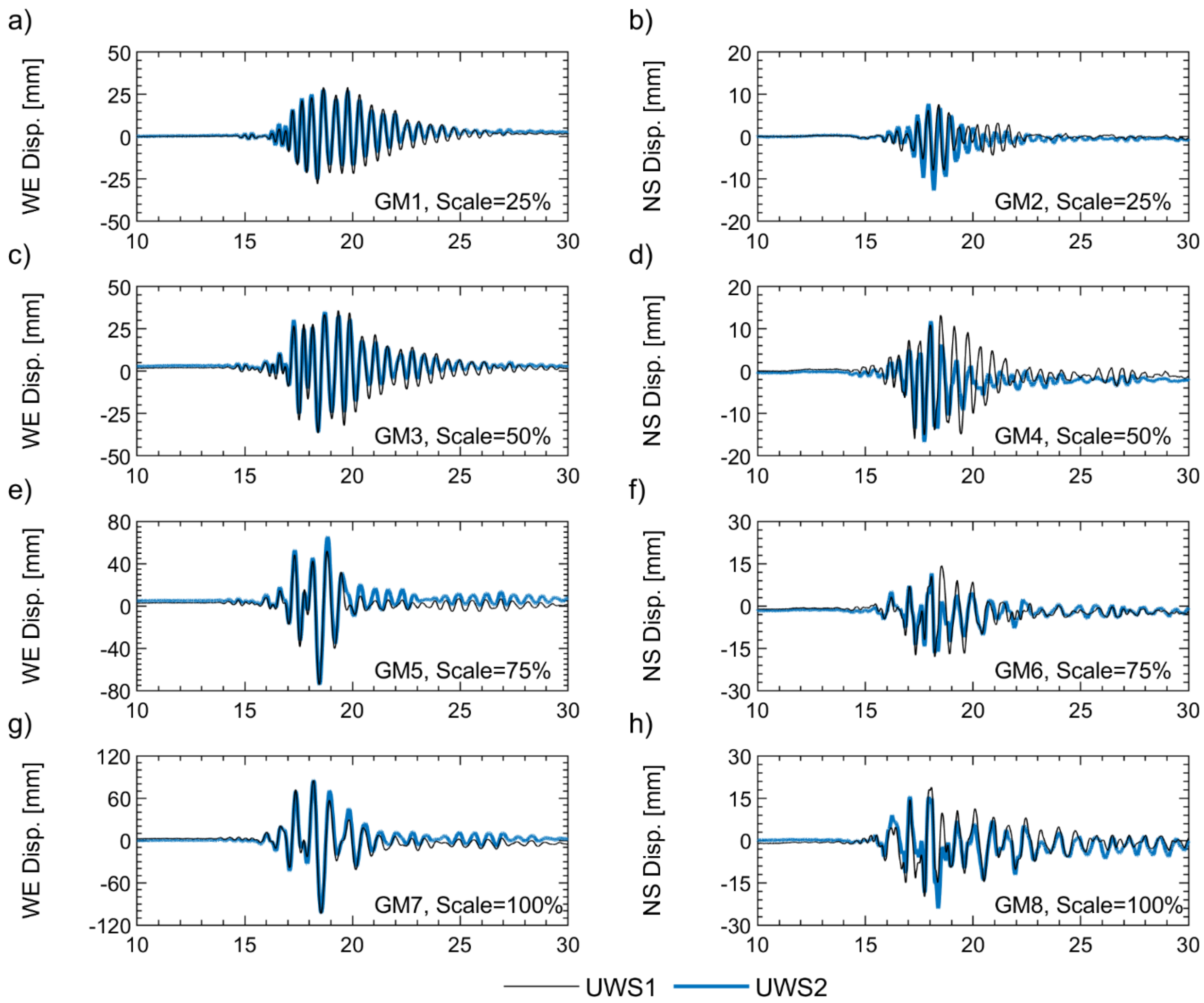

Figure 11 Displacement time-histories for units UWS1 and UWS2. "WE Disp." and "NS Disp." is short for west-east and north-south displacement, respectively.

EXAMPLE PLOTS OF LOCAL BEHAVIOUR

The distributed fiber-optic sensors (DFOS) were used to measure longitudinal rebar strains. Figure 12a presents the longitudinal strain profiles of the instrumented rebar in the north flange boundary end (see Figure 1) of UWS1 during GM1. The strain profiles are shown for two key instances: (1) when the wall experiences its largest displacement towards the east, resulting in compression, and (2) when the wall experiences its largest displacement towards the west, resulting in tension.

The results in Figure 12a confirm that, under these input motions, the wall remains in a cracked-elastic state. The largest tensile strains at the base of the north flange boundary end reach approximately 1.4 mm/m (0.14%), which is about half the strain required for steel yielding. Notably, a small increase in compressive strains is observed at approximately 1.5 m above the foundation, aligning with the height of the first-story intermediate slab (see Figure 2). This may result from increased axial force in the boundary element due to the flexural response and the coupling effect of the intermediate slab (Janevski & Isaković, 2025).

In contrast, Figure 12b presents the longitudinal strain profiles from the OptiTrack data corresponding to the maximum wall displacement towards the east and west under GM7. The tracking markers for OptiTrack were attached to the outer surface of the north flange, approximately 75 mm from the boundary end edge, with a vertical spacing of ~150 mm, though minor height variations existed because of the intermediate slabs. These results indicate an inelastic response, as expected. The tensile strain profiles align well with observed crack patterns on the south flange (Figure 12a). A key limitation of using "spot sensors" (Hoult *et al.*, 2023a), such as the OptiTrack passive markers used in this study, is their inability to directly measure strain penetration into the foundation—unlike the DFOS in Figure 12a.

These figures can be reproduced using the "DFOS_UWS1_GM1.m" and "OptiTrack_UWS1_GM7.m" MATLAB scripts, located in the primary DATA folder (see Figure 10). Regarding the latter file, two MATLAB functions are also needed to run the script, "OptiTrack_reader.m" and "importOptiTrackCSVfile.m". The data files used to generate these plots can be found in the DATA / UWS(i) / Processed_Data / DFOS and OptiTrack subfolders.

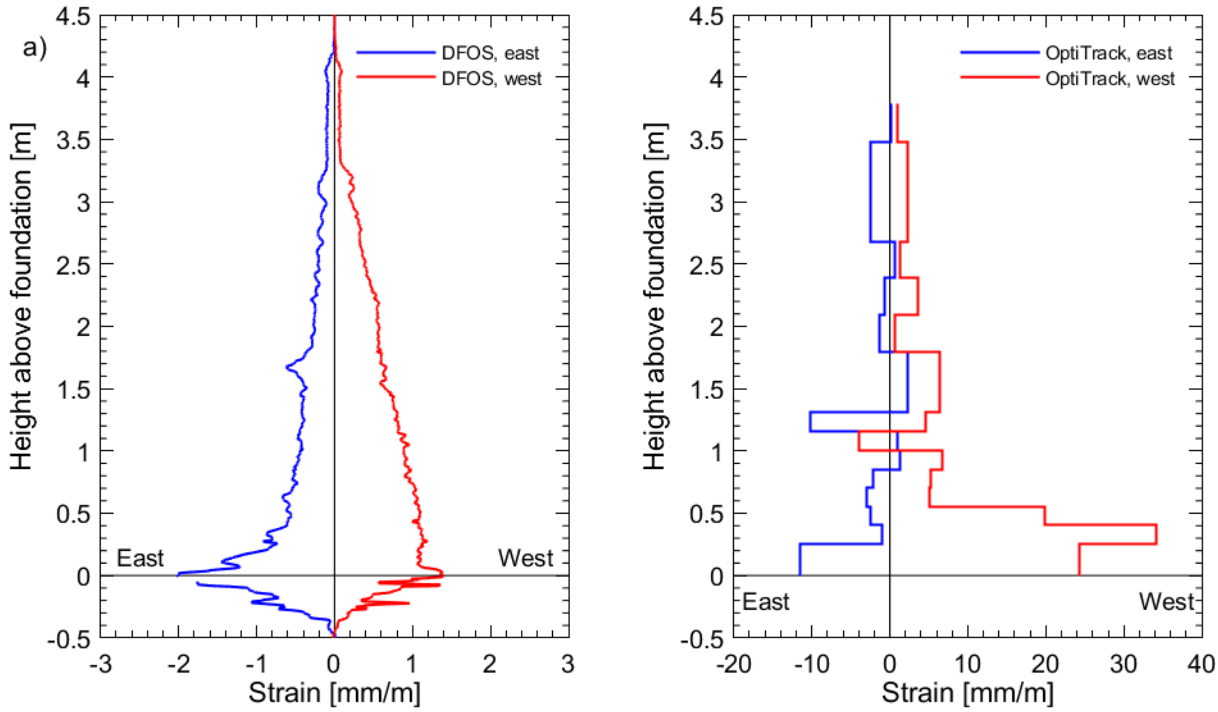

Figure 12 Longitudinal (Vertical) strain profiles for UWS1 measured from (a) DFOS of steel bar in north flange boundary end during GM1 (b) OptiTrack during GM7 corresponding to the largest west-east displacement.

SUMMARY

An experimental campaign was conducted to test two large-scale RC U-shaped core wall units. The first wall, UWS1, was reinforced with conventional steel, while the second wall, UWS2, incorporated iron-based shape memory alloys (FeSMAs). The primary objectives were to investigate the flexural and torsional behavior of these walls and to assess their residual displacements. These aspects will be explored in more detail in subsequent publications, as the current paper primarily focuses on the data repository.

Failure of both test units occurred during the largest uni- and bi-directional ground motions (GM7 and GM8), with flange boundary end crushing accompanied by longitudinal reinforcement buckling. The crushing zone in UWS2 was larger than in UWS1 under the same loading conditions, likely due to increased north-south displacement and torsional rotation demands. However, UWS2 exhibited far less flexural cracking and shear sliding compared to UWS1. This reduction in cracking was likely due to precompression applied through temperature-induced activation of the FeSMAs and partial debonding of the FeSMAs over the first (ground) story.

The wall units were extensively instrumented with conventional sensors alongside state-of-the-practice measurement technologies, including digital image correlation, video tracking of painted targets, motion capture, and distributed fiber-optic sensors. The corresponding data has been made publicly available through the UCLouvain open repository, Dataverse (https://doi.org/10.14428/DVN/MSDSWS).

Publicly accessible datasets, such as those presented in this study, are crucial for advancing the understanding of RC wall behavior and for validating future numerical models.

ACKNOWLEDGMENTS

This work is part of the transnational access project "ERIES–ALL4wALL", supported by the Engineering Research Infrastructures for European Synergies (ERIES) project (http://www.eries.eu), which has received funding from the European Union's Horizon Europe Framework Programme under Grant Agreement No. 101058684. This is ERIES publication number D4. The iron-based shape memory alloys are part of a project that has received funding from the European Union's Horizon 2020 research and innovation programme under the Marie Skłodowska-Curie grant agreement number 101061439. The authors thank Susana Almeida and Artur Santos from the Earthquake Engineering and Structural Dynamics Unit (NESDE) at the National Laboratory for Civil Engineering (LNEC) for their invaluable support in facilitating these tests. We also extend our gratitude to Fernando Oliveira for his prompt assistance in resolving data acquisition issues early in the testing process. Additionally, we thank Vincent Forzee from the Mechanical Testing, Structures, and Civil Engineering Laboratory (LEMSC) at Université catholique de Louvain for his invaluable contributions. The authors also thank those who reviewed the manuscript before submission, including Prof. Aude Simar from the Université catholique de Louvain, whose support has been instrumental to this project from the beginning.

CONTRIBUTIONS

Ryan Hoult: Conceptualization, Methodology, Investigation, Resources, Data Curation, Writing - Original Draft, Visualization; **João Pacheco de Almeida**: Conceptualization, Methodology, Investigation, Resources, Writing - Review & Editing, Supervision, Funding acquisition; **Alex Bertholet**: Conceptualization, Methodology, Validation, Investigation; **Paulo Candeias**: Investigation, Resources; **Gwendal Cumunel**: Investigation, Resources, Formal Analysis, Software; **Catherine Doneux**: Resources; **Denis Garnier**: Resources, Investigation; **Yunyeok Han**: Formal Analysis, Resources, Investigation; **Tatjana Isakovic**: Conceptualization, Resources, Methodology; **Antonio Janevski**: Methodology, Validation, Formal Analysis; **Stefania Lo Feudo**: Formal Analysis, Resources, Investigation; **Andrea Orgnoni**: Methodology, Validation, Formal Analysis; **Basile Payen**: Methodology, Validation, Formal

Analysis; **Dan Palermo**: Conceptualization, Methodology; **Rui Pinho**: Conceptualization, Methodology; **Filipe Ribeiro**: Investigation, Resources; **António Araújo Correia**: Conceptualization, Methodology, Investigation, Resources, Validation, Formal Analysis, Software.

CONFLICT OF INTEREST

The authors declare that they have no conflicts of interest to disclose.

DATA AND RESOURCES

The data generated from these dynamic tests, and used to produce the example plots presented herein, are available in Hoult *et al.* (2025a).

REFERENCES

ACI. (2019). *ACI CODE-318-19(22): Building Code Requirements for Structural Concrete and Commentary (Reapproved 2022)*. Farmington Hills, MI: American Concrete Institute.

Almeida, J. P. d., & Hoult, R. (2025). *Seismic Residual Displacements of RC U-shaped Core Walls: Preliminary Findings*. Paper presented at the 2025 International Workshop in Engineering Research Infrastructures for European Synergies (ERIES-IW2025), Lisbon, Portugal.

Almeida, J. P. d., Hoult, R., Bertholet, A., Candeias, P., Carvalho, A., Correia, A. A., . . . Sousa, M. L. (2024). *Shake-Table Testing of Two U-Shaped RC Walls: Overview of the Project ERIES-ALL4wALL*. Paper presented at the 8th World Conference on Earthquake Engineering (WCEE2024), Milan, Italy.

Andrew, R. M. (2018). Global CO2 emissions from cement production. *Earth System Science Data, 10*, 195-217. doi:https://doi.org/10.5194/essd-10-195-2018, 2018.

Bado, M. F., Casas, J. R., Dey, A., & Berrocal, C. G. (2020). Distributed Optical Fiber Sensing Bonding Techniques Performance for Embedment inside Reinforced Concrete Structures. *Sensors, 20*(20), 5788. doi:https://doi.org/10.3390/s20205788

Barrias, A., Casas, J. R., & Villalba, S. (2018). Embedded Distributed Optical Fiber Sensors in Reinforced Concrete Structures—A Case Study. *Sensors, 18*(4), 980. doi:https://doi.org/10.3390/s18040980

Berrocal, C. G., Fernandez, I., & Rempling, R. (2021). Crack monitoring in reinforced concrete beams by distributed optical fiber sensors. *Structure and Infrastructure Engineering, 17*(1), 124-139. doi:https://doi.org/10.1080/15732479.2020.1731558

Beyer, K., Dazio, A., & Priestley, M. J. N. (2008). Quasi-Static Cyclic Tests of Two U-Shaped Reinforced Concrete Walls. *Journal of Earthquake Engineering, 12*(7), 1023-1053. doi:https://doi.org/10.1080/13632460802003272

BSI. (2009). Stainless steel bars for the reinforcement of and use in concrete — Requirements and test methods. In: British Standards BS 6744:2001 + A2:2009: 28.

Candeias, P. X., Correia, A. A., & Tekeste, G. G. (2023). Shake Table Testing Techniques: Current Challenges and New Trends. In C. Chastre, J. Neves, D. Ribeiro, M. G. Neves, & P. Faria (Eds.), *Advances on Testing and Experimentation in Civil Engineering: Materials, Structures and Buildings* (pp. 173-197). Cham: Springer International Publishing.

CEN. (2004a). Eurocode 2: Design of concrete structures, Part 1-1, EN 1992-1-1. In.

CEN. (2004b). Eurocode 8: Design of structures for earthquake resistance. Part 1, EN 1998-1. In.

CEN. (2005). Eurocode 8: Design of structures for earthquake resistance - Part 3: Assessment and retrofitting of buildings. In.

Cheloni, D., De Novellis, V., Albano, M., Antonioli, A., Anzidei, M., Atzori, S., . . . Doglioni, C. (2017). Geodetic model of the 2016 Central Italy earthquake sequence inferred from InSAR and GPS data. *Geophysical Research Letters, 44*(13). doi:https://doi.org/10.1002/2017GL073580

Constantin, R., & Beyer, K. (2016). Behaviour of U-shaped RC walls under quasi-static cyclic diagonal loading. *Engineering Structures, 106*, 36-52. doi:https://doi.org/10.1016/j.engstruct.2015.10.018

Fawaz, G., & Murcia-Delso, J. (2020). Bond behavior of iron-based shape memory alloy reinforcing bars embedded in concrete. *Materials and Structures, 53*(5), 114. doi:https://doi.org/10.1617/s11527-020-01548-y

Flatt, R. J., Roussel, N., & Cheeseman, C. R. (2012). Concrete: An eco material that needs to be improved. *Journal of the European Ceramic Society, 32*(11), 2787-2798. doi:https://doi.org/10.1016/j.jeurceramsoc.2011.11.012

Gu, X.-L., Chen, Z.-Y., Yu, Q.-Q., & Ghafoori, E. (2021). Stress recovery behavior of an Fe-Mn-Si shape memory alloy. *Engineering Structures, 243*. doi:https://doi.org/10.1016/j.engstruct.2021.112710

Hoult, R. (2021). Torsional capacity of reinforced concrete U-shaped walls. *Structures, 31*, 190-204. doi:https://doi.org/10.1016/j.istruc.2021.01.104

Hoult, R., & Almeida, J. P. d. (2024a). Flexure-Torsion Response of Compressed Open Reinforced-Concrete Cores: Experimental Strain Gradients, Numerical Methods, and Interaction Diagrams. *Journal of Structural Engineering*. doi:https://doi.org/10.1061/JSENDH.STENG-13147

Hoult, R., & Almeida, J. P. d. (2024b). Modified compression field theory and disturbed stress field model on the simulation of the global and local behaviour of non-planar reinforced concrete walls under cyclic and dynamic loading. *Bulletin of Earthquake Engineering*. doi:https://doi.org/10.1007/s10518-024-01982-1

Hoult, R., & Almeida, J. P. d. (2024c). *Ongoing Experimental Programmes on RC Walls Reinforced with Iron-Based Shape Memory Alloy Rebars*. Paper presented at the 8th World Conference on Earthquake Engineering (WCEE2024), Milan, Italy.

Hoult, R., Almeida, J. P. d., Correia, A. A., Candeias, P. X., Cumunel, G., Han, Y., . . . Archez, J. (2025a). *Dataset: Shake-table Tests on Two 40-ton Reinforced Concrete U-shaped Walls with Uniaxial and Bidirectional-torsional Response*. doi:https://doi.org/10.14428/DVN/MSDSWS

Hoult, R., Appelle, A., Almeida, J., & Beyer, K. (2020). Seismic performance of slender RC U-shaped walls with a single-layer of reinforcement. *Engineering Structures, 225*. doi:https://doi.org/10.1016/j.engstruct.2020.111257

Hoult, R., Bertholet, A., & Almeida, J. P. d. (2023a). Core versus Surface Sensors for Reinforced Concrete Structures: A Comparison of Fiber-Optic Strain Sensing to Conventional Instrumentation. *Sensors, 23*(3), 1745. doi:https://doi.org/10.3390/s23031745

Hoult, R., & Beyer, K. (2020). Decay of Torsional Stiffness in RC U-Shaped Walls. *Journal of Structural Engineering, 146*(9). doi:https://doi.org/10.1061/(ASCE)ST.1943-541X.0002733

Hoult, R., Doneux, C., & Pacheco de Almeida, J. (2023b). Tests on reinforced concrete U-shaped walls subjected to torsion and flexure. *Earthquake Spectra, 39*(4), 2685-2710. doi:https://doi.org/10.1177/87552930231195315

Hoult, R., Janevski, A., Orgnoni, A., Almeida, J. P. d., Isakovic, T., & Pinho, R. (2025b). Evaluating State-of-the-Art Models for RC Core Walls with Torsion. *Submitted to ACI Structural Journal*.

Hoult, R. D., & Almeida, J. P. d. (2022). Residual displacements of reinforced concrete walls detailed with conventional steel and shape memory alloy rebars. *Engineering Structures, 256*, 114002. doi:https://doi.org/10.1016/j.engstruct.2022.114002

Hoult, R. D., Lumantarna, E., & Goldsworthy, H. M. (2015, 6-8 November, 2015). *Torsional Displacement for Asymmetric Low-Rise Buildings with RC C-shaped Cores.* Paper presented at the Proceedings of the Tenth Pacific Conference on Earthquake Engineering, Sydney, Australia.

Ile, N., Plumier, C., & Reynouard, J. M. (2002). *Test program on U-shaped walls leading to model validation and implications to design.* Paper presented at the 12th European Conference on Earthquake Engineering, London, England.

Ile, N., & Reynouard, J. M. (2005). Behaviour of U-shaped Walls Subjected to Uniaxial and Biaxial Cyclic Lateral Loading. *Journal of Earthquake Engineering, 09*(01), 67-94.

Isaković, T., Gams, M., Janevski, A., Rakićević, Z., Bogdanović, A., Jekić, G., . . . Fischinger, M. (2021). Shake table test of RC walls' coupling provided by slabs. *Građevinski materijali i konstrukcije, 64*(4), 225-234. doi:https://doi.org/10.5937/grmk2104225i

Janevski, A., & Isaković, T. (2025). Seismic response of RC walls coupled by slabs without coupling beams. *Engineering Structures, 329*. doi:https://doi.org/10.1016/j.engstruct.2025.119861

Kawashima, K., & Tirasit, P. (2008). Effect of Nonlinear Seismic Torsion on the Performance of Skewed Bridge Piers. *Journal of Earthquake Engineering, 12*(6), 980-998. doi:https://doi.org/10.1080/13632460701673019

Liossatou, E., & Fardis, M. N. (2015). Residual displacements of RC structures as SDOF systems. *Earthquake Engineering & Structural Dynamics, 44*(5), 713-734. doi:https://doi.org/10.1002/eqe.2483

Liu, Z., Dong, Z., Sun, Y., Zhu, H., Wu, G., Sun, C., & Soh, C.-K. (2023). Effect of resistive heating on the bond properties between iron-based shape memory bars and cement mortar. *Journal of Building Engineering, 66*. doi:https://doi.org/10.1016/j.jobe.2023.105895

Lo Feudo, S., Han, Y., Cumunel, G., Hoult, R., Bertholet, A., Garnier, D., . . . Almeida, J. P. d. (2025). Video tracking of targets for vibration measurement of large-scale structures under seismic excitation. *Earthquake Engineering & Structural Dynamics, 54*, 2106-2120.

Luzi, L., Lanzano, G., Felicetta, C., D'Amico, M. C., Russo, E., Sgobba, S., . . . ORFEUS Working Group 5. (2020). *Engineering Strong Motion Database (ESM) (Version 2.0)*. doi:https://doi.org/10.13127/ESM.2

Mahin, S. A., & Bertero, V. V. (1981). An Evaluation of Inelastic Seismic Design Spectra. *Journal of the Structural Division, 107*(9), 1777-1795. doi:https://doi.org/10.1061/JSDEAG.0005782

Mália, M., de Brito, J., Pinheiro, M. D., & Bravo, M. (2013). Construction and demolition waste indicators. *Waste Management & Research, 31*(3), 241-255. doi:https://doi.org/10.1177/0734242x12471707

Marquis, F., Kim, J. J., Elwood, K. J., & Chang, S. E. (2017). Understanding post-earthquake decisions on multi-storey concrete buildings in Christchurch, New Zealand. *Bulletin of Earthquake Engineering, 15*(2), 731-758. doi:https://doi.org/10.1007/s10518-015-9772-8

Maruta, M., Suzuki, N., Miyashita, T., & Nishioka, T. (2000). *Structural capacities of H-shaped RC core wall subjected to lateral load and torsion.* Paper presented at the Proceedings of the 12th WCEE. New Zealand: The New Zealand Society for Earthquake Engineering.

McCormick, J., Aburano, H., Ikenaga, M., & Nakashima, M. (2008). *Permissible residual deformation levels for building structures considering both safety and human elements.* Paper presented at the 14th world conference on earthquake engineering, Beijing, China.

Michels, J., Shahverdi, M., & Czaderski, C. (2018). Flexural strengthening of structural concrete with iron-based shape memory alloy strips. *Structural Concrete, 19*(3), 876-891. doi:https://doi.org/10.1002/suco.201700120

Michou, A., Hilaire, A., Benboudjema, F., Nahas, G., Wyniecki, P., & Berthaud, Y. (2015). Reinforcement–concrete bond behavior: Experimentation in drying conditions and meso-scale modeling. *Engineering Structures, 101*, 570-582. doi:https://doi.org/10.1016/j.engstruct.2015.07.028

Muir-Wood, R. (2015). The Christchurch earthquakes of 2010 and 2011. The Geneva risk reports. Risk and insurance research. Extreme events and insurance: 2011 Annus horribilis. Courbage C, Stahel WR, Geneva. In.

Orgnoni, A. (2025). *Accurate and Computationally Affordable Estimation of the Global and Local Response of RC Wall Cores Subjected to Seismic Loading.* (PhD). Scuola Universitaria Superiore IUSS Pavia, Pavia, Italy.

Peng, X.-N., & Wong, Y.-L. (2011). Behavior of reinforced concrete walls subjected to monotonic pure torsion—An experimental study. *Engineering Structures, 33*(9), 2495-2508. doi:https://doi.org/10.1016/j.engstruct.2011.04.022

Pinho, R. (2000). Shaking table testing of RC walls. *ISET Journal of Earthquake Technology, 37*(4), 119-142.

Quiertant, M., Baby, F., Khadour, A., Marchand, P., Rivillon, P., Billo, J., . . . Cordier, J. (2012, May 22-24). *Deformation monitoring of reinforcement bars with a distributed fiber optic sensor for the SHM of* *reinforced concrete structures*. Paper presented at the 9th International Conference on NDE in Relation to Structural Integrity for Nuclear and Pressurized Components, Seattle, Washington, USA.

Raza, S., Michels, J., Schranz, B., & Shahverdi, M. (2022a). Anchorage behavior of Fe-SMA rebars Post-Installed into concrete. *Engineering Structures, 272*. doi:https://doi.org/10.1016/j.engstruct.2022.114960

Raza, S., Shafei, B., Saiid Saiidi, M., Motavalli, M., & Shahverdi, M. (2022b). Shape memory alloy reinforcement for strengthening and self-centering of concrete structures—State of the art. *Construction and Building Materials, 324*. doi:https://doi.org/10.1016/j.conbuildmat.2022.126628

Raza, S., Widmann, R., Michels, J., Saiid Saiidi, M., Motavalli, M., & Shahverdi, M. (2023). Self-centering technique for existing concrete bridge columns using prestressed iron-based shape memory alloy reinforcement. *Engineering Structures, 294*. doi:https://doi.org/10.1016/j.engstruct.2023.116799

re-fer. (2025). re-bar method for concrete structures. Retrieved from https://www.re-fer.eu/en/re-bar/

Sextos, A., De Risi, R., Pagliaroli, A., Foti, S., Passeri, F., Ausilio, E., . . . Zimmaro, P. (2018). Local Site Effects and Incremental Damage of Buildings during the 2016 Central Italy Earthquake Sequence. *Earthquake Spectra, 34*(4). doi:https://doi.org/10.1193/100317eqs194m

Shahverdi, M., Michels, J., Czaderski, C., & Motavalli, M. (2018). Iron-based shape memory alloy strips for strengthening RC members: Material behavior and characterization. *Construction and Building Materials, 173*. doi:https://doi.org/10.1016/j.conbuildmat.2018.04.057

Smil, V. (2013). *Making the modern world: materials and dematerialization*: John Wiley & Sons.

Soroushian, P., Ostowari, K., Nossoni, A., & Chowdhury, H. (2001). Repair and Strengthening of Concrete Structures Through Application of Corrective Posttensioning Forces with Shape Memory Alloys. *Transportation Research Record, 1770*(1), 20-26. doi:https://doi.org/10.3141/1770-03

Sritharan, S., Beyer, K., Henry, R. S., Chai, Y. H., Kowalsky, M., & Bull, D. (2014). Understanding Poor Seismic Performance of Concrete Walls and Design Implications. *Earthquake Spectra, 30*(1), 307-334. doi:https://doi.org/10.1193/021713EQS036M

Standards Association NZ. (2006). NZS 3101: Part1:2006, "Concrete Structures Standard - The Design of Concrete Structures". In.

Stewart, J. P., Zimmaro, P., Lanzo, G., Mazzoni, S., Ausilio, E., Aversa, S., . . . Tropeano, G. (2018). Reconnaissance of 2016 Central Italy Earthquake Sequence. *Earthquake Spectra, 34*(4), 1547-1555. doi:https://doi.org/10.1193/080317eqs151m

Türkay, A., & Altun, F. (2022). Experimental study of seismic torsional behavior of reinforced concrete walls. *Bulletin of Earthquake Engineering*. doi:https://doi.org/10.1007/s10518-022-01366-3

UN Environment. (2017). *Global Status Report 2017: Towards a zero-emission, efficient, and resilient building and construction sector*. Retrieved from www.globalabc.org

United Nations. (2025). Department of Economic and Social Affairs, Sustainable Development. Retrieved from https://sdgs.un.org/

Vahedi, M., Zolfagharysaravi, S., Ebrahimian, H., & Saiid Saiidi, M. (2024). Experimental-analytical investigation of accelerated bridge construction concrete columns with self-centering Fe-SMA bars subjected to near-fault ground motions. *Engineering Structures, 299*. doi:https://doi.org/10.1016/j.engstruct.2023.117127

Varsamis, C. D., & Papanikolaou, V. K. (2021). Evaluation of current Eurocode 8 provisions on R/C ductile wall design. *Structures, 33*, 368-377. doi:https://doi.org/10.1016/j.istruc.2021.04.072

Zhang, S., Liu, H., Coulibaly, A. A. S., & DeJong, M. (2021). Fiber optic sensing of concrete cracking and rebar deformation using several types of cable. *Structural Control and Health Monitoring, 28*(2), e2664. doi:https://doi.org/10.1002/stc.2664